이학박사학위논문

Study on Multiplexed Immunoassay Platform Using Surface Enhanced Raman Spectroscopic Nanoprobes

표면 증강 라만 분광 나노프로브를 이용한 다중 면역분석에 관한 연구

2016년 8월

서울대학교 대학원

과학교육과 화학전공

장 혜 진

Study on Multiplexed Immunoassay Platform Using Surface Enhanced Raman Spectroscopic Nanoprobes

표면 증강 라만 분광 나노프로브를 이용한

다중 면역 분석에 관한 연구

지도 교수 정 대 홍

이 논문을 이학박사학위논문으로 제출함

2016년 6월

서울대학교 대학원

과학교육과 화학전공

장 혜 진

장혜진의 이학박사학위논문을 인준함

2016년 6월

위 원 장 _____ (인)

부위원장 _____ (인)

위 원 _____ (인)

위 원 _____ (인)

위 원 _____ (인)

ABSTRACT

Study on Multiplexed Immunoassay Platform Using Surface Enhanced Raman Spectroscopic Nanoprobes

(Supervisor: Dae Hong Jeong, Ph.D.)

Hyejin Chang

Department of Science Education

(Major in Chemistry)

The Graduate School

Seoul National University

Recently, surface-enhanced Raman scattering (SERS)-based immunoassays (SIA) have drawn much attention as diagnostic tools with large multiplex capacity and high sensitivity. However, several challenges—such as a low reproducibility, a time-consuming readout process, and limited dynamic range—remain. In this study, we demonstrated a reliable and sensitive SIA platform for prostate specific antigen (PSA) detection. Reliability and sensitivity were achieved by two approaches: 1) well-established SERS probes, so-called SERS dots that have high sensitivity (single particle detection) and little particle-to-particle variation in SERS intensity; and 2) a whole area-scanning readout method for rapid and reliable chip analysis rather than point scanning. Therefore, this thesis is composed of three chapters,

related to SERS nanoprobes for multiplexed and quantitative analysis, a sensitive and reliable readout method for 2-dimensional chip analysis, and immunoassay platform as a whole of former two, respectively.

In chapter I, multiplexed and quantitative SERS nanoprobes for biological application were developed. An well-developed SERS nanoprobe, SERS dot^{TM}, was anlayzed at single particle level for characterization of sensitivity, particle-to-particle distribution of signals, and photostability for its application to immunoassay. And also, an Ag shell-Au satellite (Ag-Au SS) nanostructure composed of an Ag shell and surrounding Au nanoparticles was described as a near-IR active SERS probe. It was a key strategy to create isotropic hot spots in developing a reproducible, homogeneous, and ultra-sensitive SERS probe. The heterometallic shell-satellite structure based SERS probe produced an intense and uniform SERS signals (SERS enhancement factor: ~1.4×10^6 with 11% relative standard deviation) with high detectability (100% under our measurement condition) by 785-nm photoexcitation. This signal enhancement was independent of the laser polarizations, which reflects the isotropic feature of the SERS activity of Ag-Au SS from the three-dimensional (3-D) distribution of SERS hot spots between the shell and the surrounding satellite particles. The Ag-Au SS nanostructure shows a great potential as a reproducible and quantifiable SERS probe for biological targets.

In Chapter II, a whole area scanning readout method for rapid and reliable chip analysis was described. SERS techniques have been widely used for bioanalysis due to its high sensitivity and multiplex capacity. However, the point-scanning method using a micro-Raman system, which is the most common method in the

literature, has a disadvantage of extremely long measurement time for on-chip immunoassay adopting a large chip area of approximately 1-mm scale and confocal beam point of ca. 1-μm size. Alternative methods such as sampled spot scan with high confocality and large-area scan method with enlarged field of view and low confocality have been utilized in order to minimize the measurement time practically. In this study, we analyzed the two methods in respect of signal-to-noise ratio and sampling-led signal fluctuations to obtain insights on a fast and reliable readout strategy. On this basis, we proposed a methodology for fast and reliable quantitative measurement of the whole chip area. The proposed method adopted a raster scan covering a full area of 100 μm × 100 μm region as a proof-of-concept experiment while accumulating signals in the CCD detector for single spectrum per frame. One single scan with 10 s over 100 μm × 100 μm area yielded much higher sensitivity compared to sampled spot scanning measurements and no signal fluctuations attributed to sampled spot scan. This readout method is able to serve as one of key technologies that will bring quantitative multiplexed detection and analysis into practice.

In chapter III, a reliable and reproducible chip-based SERS immunoassay with high sensitivity and broad dynamic range was described. It was achieved by using the reproducible nanoprobes with single-particle sensitivity (SERS dot), and the reliable readout method from sub-millimeter area. As a feasibility test, PSA analysis was performed as a model system. Bio-functionality of SERS dot was demonstrated, and the number of antibody on the silica surface and captured antigens were evaluated by utilizing fluorescence-labeled antibody and antigen. Finally, PSA could be detected with high sensitivity (*ca*. 0.11 pg/mL, 3.4 fM LOD),

with a wide dynamic range (0.001−1000 ng/mL). In addition, the developed platform was successfully adopted to detect PSA in the patient's serum. Thus, the developed platform will facilitate development of reliable immunoassays with high sensitivity and a wide dynamic range.

Keywords: Surface-enhanced Raman scattering (SERS), immunoassay, prostate specific antigen (PSA), SERS nanoprobe, core-satellite, SERS hot spot, near-infrared probe, uniform SERS activity, quantitative analysis, area-scanning, on-chip analysis, sensitivity, reproducibility

Student number: 2011-21586

TABLE OF CONTENTS

LIST OF TABLES

LIST OF FIGURES

Introduction

Chapter I.

Chapter III.

LIST OF ABBREVIATIONS

4-BBT	4-bromobenzenethiol
4-CBT	4-chlorobenzenethiol
4-FBT	4-fluorobenzenethiol
Ab	antibody
Ag NS	silver nanoshell
Ag-Au SS	Ag shell-Au satellite type SERS nanoparticle
APTES	(3-aminopropyl) triethoxysilane
Au NP	gold nanoparticle
BOP	benzotriazol-1-yloxy-tris(dimethylamino) phosphonium hexafluorophsphate
BSA	bovine serum albumin
CCD	charge-coupled device
CLIA	chemi-luminescence immunoassay
DI water	deionized water
DIEA	*N,N′*-diisopropylethylamine
DMAP	4-dimethylaminopyridine
EDX	energy dispersive X-ray spectroscopy
EF	enhancement factor
ELISA	enzyme-linked immunosorbent assay
EM	electromagnetic
EtOH	ethanol
FITC	fluorescein isothiocyanate
HOBt	*N*-hydroxybenzotriazole
HR-TEM	high resolution-transmission electron microscope

IRMA	immunoradiometric assay
MPTS	3-mercaptopropyl trimethoxysilane
NIR	near-infrared
NMP	*N*-methylpyrolidone
NP	nanoparticle
PBS	phosphate buffered saline
PBST	Tween 20 in phosphate buffered saline
PEG	poly(ethylene glycol)
PSA	prostate-specific antigen
RLC	Raman label compound
RSD	relative standard deviation
SEM	scanning electron microscope
SERS	Surface-enhanced Raman scattering
SERS dot	SERS active nanoparticle
SIA	SERS based immunoassay
Si NPs	silica nanoparticles
SNR	signal-to-noise ratio
TEM	transmission electron microscope
TEOS	tetraethylorthosilicate
UV	ultraviolet
UVA	ultraviolet A
Vis	visible

Study on Multiplexed Immunoassay Platform Using Surface Enhanced Raman Spectroscopic Nanoprobes

Introduction

1. Basics of surface-enhanced Raman spectroscopy (SERS)

Raman spectroscopy provides rich vibrational information and unique Raman fingerprints from various kinds of samples. Due to easy measurements, simple preparation of sample, and non-destructive characteristics,[1] Raman spectroscopy has been considered an attractive analytical technique. However, Raman scattering have inherently weak signals,[2] therefore resulting in a poor sensitivity and limited application of Raman spectroscopy. This challenge originates in the extremely small cross section of inelastic scattering. However, since Fleischmann *et al.* observed enhanced Raman signal of pyridine absorbed on rough silver surface in 1973 (and reported in 1974),[3] this phenomenon, so called surface-enhanced Raman scattering (SERS), has boosted great attentions in Raman spectroscopy. Commonly, two mechanisms are accepted for explaining the SERS effect: the electromagnetic (EM) effect, and chemical enhancement.[4] The dominant contribution arises from the EM enhancement involving field enhancement on the nanostructured metallic surfaces by plasmon resonance excitations.[5-6]

The researches in SERS have been dramatically increased due to the advances in nanotechnology and improvement in instrumental techniques.[1]

Substantial studies have focused on the fabrication of SERS-active substrates and its applications to many fields, including surface, analytical and biological researches. Because the application depends on the activity and reproducibility of the substrate, the key step for practical application of SERS is still the success in fabrication of the SERS substrate including control the hot spots.

The current SERS-based methods are generally devided into two categories:[5,7-8] the direct sensing of analytes (label-free detection), and targeted research with SERS labels, so called SERS nanoprobes. The SERS nanoparticle (NP) based nanoprobe technologies provide high sensitivity for trace analysis with fine designing.[9-12] And due to the nature of Raman scattering such as the narrow line widths, and non-photobleaching characteristics, SERS nanoprobes are inherently sutable for multiplex analysis with high photostability.[2,5-6,13-16] Furthermore, optically tuned nanostructures enable utilization of near-infrared (NIR) excitation to minimize the autofluorescent background from biological samples, achieving *in vivo* application of SERS nanoprobes for noninvasive imaging.[17-18] For these merits of SERS nanoprobes, the development of SERS nanoprobe are widely considered a significant advance in nanobiotechnology.

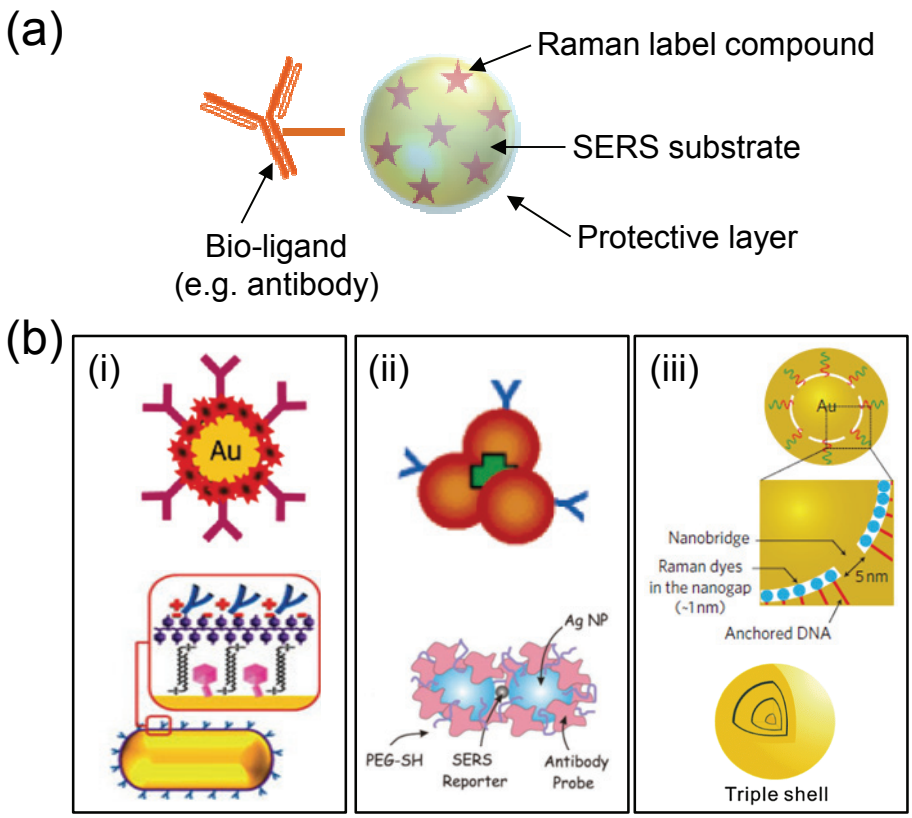

Figure 1. Various SERS nanoprobes.

Schematic illustrations of (a) typical SERS nanoprobes composed of SERS substrate, Raman label compound, protective shell and bioligand, and (b) various examples of SERS nanoprobes: (i) single gold nanoparticle types,[19-20] (ii) aggregated or dimerized nanoparticles,[10,21] and (iii) nanoparticles containing the internal gaps.[22-23]

2. Development of SERS nanoprobes

The SERS nanoprobes which are functionalized metal nanoparticles for targeted reasearch typically contain four components (Figure 1a):[5-6,8] 1) a SERS substrate which is usually noble metal nanoparticle, 2) Raman label molecules attached on the surface, 3) protective layer for biocomparability, antiaggregation, and further surface modification and 4) biomolecules as bio-ligand for target-specific detection. SERS nanoprobes are designed to produce strong, and unique Raman signals, therefore used for indirect sensing of target molecules.

2. 1. Design of noble metal nanostructures as SERS nanoprobes

Single molecule-level sensitivity of surface-enhanced Raman scattering (SERS) was known approximately twenty years ago.[24-25] Ever since there have been many different applications benefiting from the ultra-high sensitivity such as single molecule detection,[26] chemical sensing,[27-28] and bio-molecular probes.[5,9,16,29-34]

Many different SERS probes have been reported for bio-molecular detection (Figure 1b). Single gold nanoparticle-based probes have been widely used by many researchers.[19-20,29,34] In order to develop sensitive SERS probes,

several approaches have been reported focusing on the synthesis of advanced nanostructures[23,26,35-41] or efficient Raman reporters which are resonant with excitation light.[42-44] Successful aggregation of silver nanoparticles (COINs) was reported and successfully applied to multiplexing in bio-systems such as tissue sample.[33] Especially, dimeric nanostructures[45-48] and small clusters[49-50] were reported as SERS probes. One of ideal structures for SERS probe is conjoined dimer of nanoparticles or small cluster of nanoparticles for SERS hot spot generation. These nanostructures could generate hot spots from nano-gap junctions between nanoparticles (NPs) where the electromagnetic field is significantly concentrated, allowing for an ultra-sensitive SERS signal.[26,51-52] However, the anisotropic structure with uncontrollable nano-gap junctions leads to signal fluctuation and dependency on incident light polarization. Therefore, for developing reproducible and homogeneous SERS probes, creating and controlling hot spots in isotropic structures is a critical issue.[23,35-36,41]

Recently, a highly uniform and reproducible SERS probe in the visible range was reported by Lim *et al*.[23] It is worth noting that signal fluctuations among SERS probes were minimal because the 1-nm gap in the interior of the SERS probe was precisely controlled by utilizing single stranded DNA. In addition, three-dimensional (3-D) core-satellite type

assembled SERS nano-probes with a uniform signal have been reported.[35-39,53-54] However, these nanosphere-based nano-gap structures and 3-D NP-assemblies are still limited for use *in vivo* applications because of their plasmonic resonance in the visible optical range where animal tissue has large absorption and auto-fluorescence. Therefore, the SERS probes which are sensitive in the near-Infrared (NIR) region, the so-called biological window, for effective *in vivo* detection and imaging of biological targets need to be developed.[18,40,55-56]

2. 2. Ensemble averaged effect: Signal homogeneity and single particle sensitivity

Usually, the nanostructures designed to have high enhancement factors (EFs) are considered as superior SERS nanoprobes. SERS EF means how many times the Raman signal per a single molecule increased by the nanostructure compared to normal Raman condition, and so far, might be a only parameter that characterizes the sensitivity of a given substrates for SERS applications. Y. Fang and co-workersreported that in EF distributions, the hottest sites (i.e., an enhancement factor > 10^9) accounted for 63 in 1,000,000 active sites, and contributed 24% to the overall SERS intensity.[51] And recently, U. D. Suh and co-workers reported that just interparticle

nanogap with distunces < 1-nm produced narrow EF value distribution.[11] These results imply that it is very difficult to get unfirom signals only from hot spot engineerings.

The EF counts especially in label free detections, however, not only the EF doesn't count practically, because the signal intensity also depends on the number of molecules which can be controlled by designing of SERS nanoprobes. The number of Raman label molecules can be controlled by controlling the concentraions and also by controlling the surface areas by uniform particle size.

The size distribution of nanoprobes can also raise issues of quantitative analysis in bio applications. For example, if the number of bio-ligand molecules on a single probe particle changed with surface area, the number of target molecules captured on the probe also changes. The varied concentration of target molecules could not give linear signal intensity with that case. Therefore, considering above two aspects, it could be a good strategy to achieve ensemble average effect by uniform and relatively large size of SERS nanoprobes for obtaining reproducible and sensitive SERS nanoprobes.

Those ensemble-averaged strategy on silica core (SERS dots) was demonstrated and evolved diversely by incorporating various functionalities

such as fluorescence and magnetism within the probe particles. [30-32] When SERS dots are fabricated from mono-dispersed SiO_2 nanoparticles, the thickness of the Ag NPs embedded on the SiO_2 surface is typically less than 10 nm, while the shell thickness can be controlled to within about 5 nm of variation. This makes it possible for the SERS dots to be essentially homogeneous in size and shape, with SEM measurement revealing that more than 75% of the NPs are monomeric.

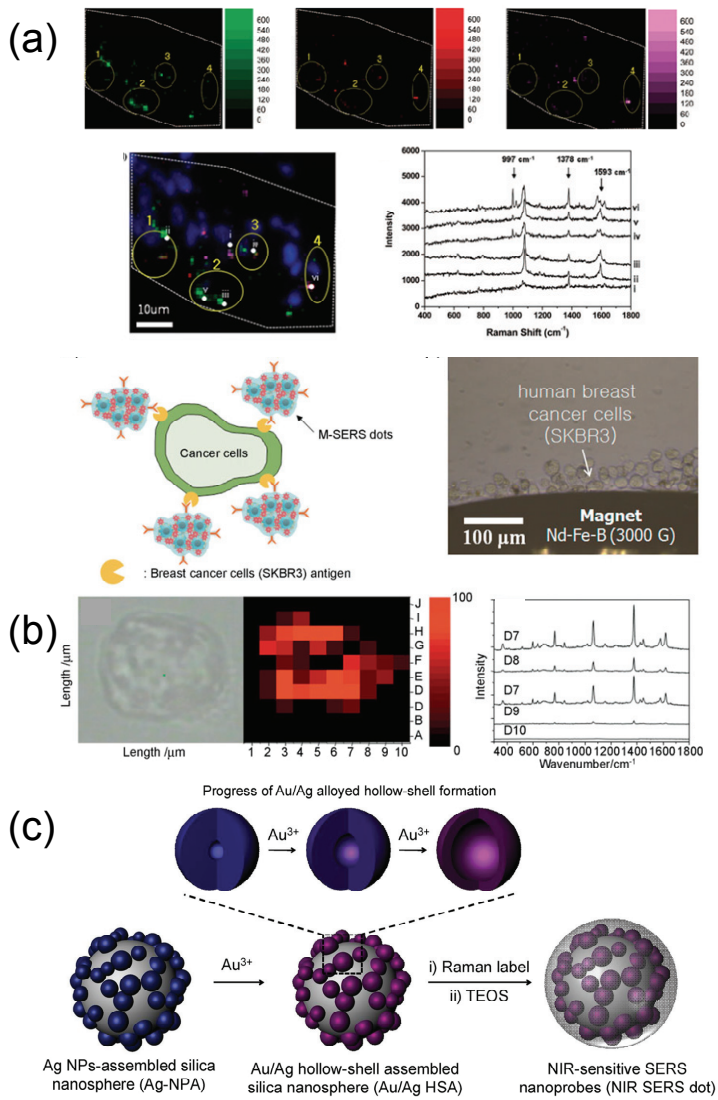

Figure 2. Various types of multifunctional SERS dot.

(a) Fluorescence-SERS multimodal nanoprobe (F-SERS dot),[31] (b) Magnetism-SERS multimpdal nanoprobe (M-SERS dot),[30] and (c) near-infrared (NIR)-sensitive SERS nanoprobe (NIR SERS dot).[18]

3. Biological applications using SERS Nanoprobes

Biofunctionalized SERS nanoprobes can be utilized in bio-applications such as *in vitro* assays or *in vivo* imaging. The target-specific biomolecule determines the selectivity: antibodies are often employed for protein (antigen) recognition. In this section, the antibodies conjugated SERS nanoprobes are mainly discussed.

3. 1. *In vitro* application of SERS nanoprobes

Recently, more advanced immunoassay platforms with various analytical backgrounds—such as surface plasmon resonance (SPR),[57] surface-enhanced Raman scattering (SERS),[58] mass spectroscopy (MS),[59] colormetric assay,[60] chemiluminescence,[61] and electrochemical methods[62] —have been invastigated. Among these techniques, SERS has drawn much attentions because of its high sensitivity, less photobleaching characteristic and multiplexing capacity.[16]

Among these techniques, SERS can be used in sensitive and efficient assays for multiple target biomarkers because of its high sensitivity, lower photobleaching and multiplexing capacity.[9,16,63] *In vitro* detections such as immunoassay,[58,64-65] pathogen detection,[66-68] and live-cell imaging[14,20,32,69] using SERS nanoprobes have been demonstrated (Figure 3). Espectially in

biomedical and clinical field, quantitative and sensitive detection of biomarkers in the blood biomarkers facilitate early diagnosis, and monitoring of disease status and progression.[70]

However, several issues—such as low signal reliability and reproducibility especially at low target concentrations,[10,71] time-consuming readout process[72-73] and limited dynamic ranges[19,71]—remain. In addition, an externally generated hot junction between the capture plate and SERS probe is needed for additional signal enhancement;[71] however, this approach inevitably involves heterogeneous SERS intensity. Therefore, there is a need to develop a SERS-based immunoassay (SIA) platform with high reliability and sensitivity.

Prostate-specific antigen (PSA), a serine protease, is used for diagnosis of carcinoma of the prostate (CaP). CaP usually causes an elevation of the blood PSA level of up to 10^5-fold (the normal cut-off value in serum is <4 ng/mL). In addition, PSA detection <0.1 ng/mL is necessary for monitoring of the response to anti-CaP drugs and recurrence in patients who underwent radical prostatectomy.[74-75] Thus, PSA diagnostic immunoassays require a broad dynamic range and high sensitivity.

Focusing on the studies targeting at PSA, Porter *et al.* reported simple SERS based immunoassays for PSA detection on the gold film substrate

using gold NPs.[34] Their sensitivity was lower than 4 pg/mL in bovine serum albumin (Figure 3). Tang *et al.* reported a highly sensitive system on the analogy of enzyme-linked immunosorbent assay (ELISA) with a detection limit below 10^{-9} ng/mL.[64] The enzyme label of ELISA blocks the dissolution of Raman reporter-labeled silver NPs through hydrogen peroxide and generated a strong Raman signal when the PSA was present (Figure 4). Still, the procedures are considered having some complexity or requiring very high costs. Choo *et al.* recently reported a microfluidic detection system for PSA detection without washing steps, and the detection limit was 0.1 ng/mL (Figure 5).[67]

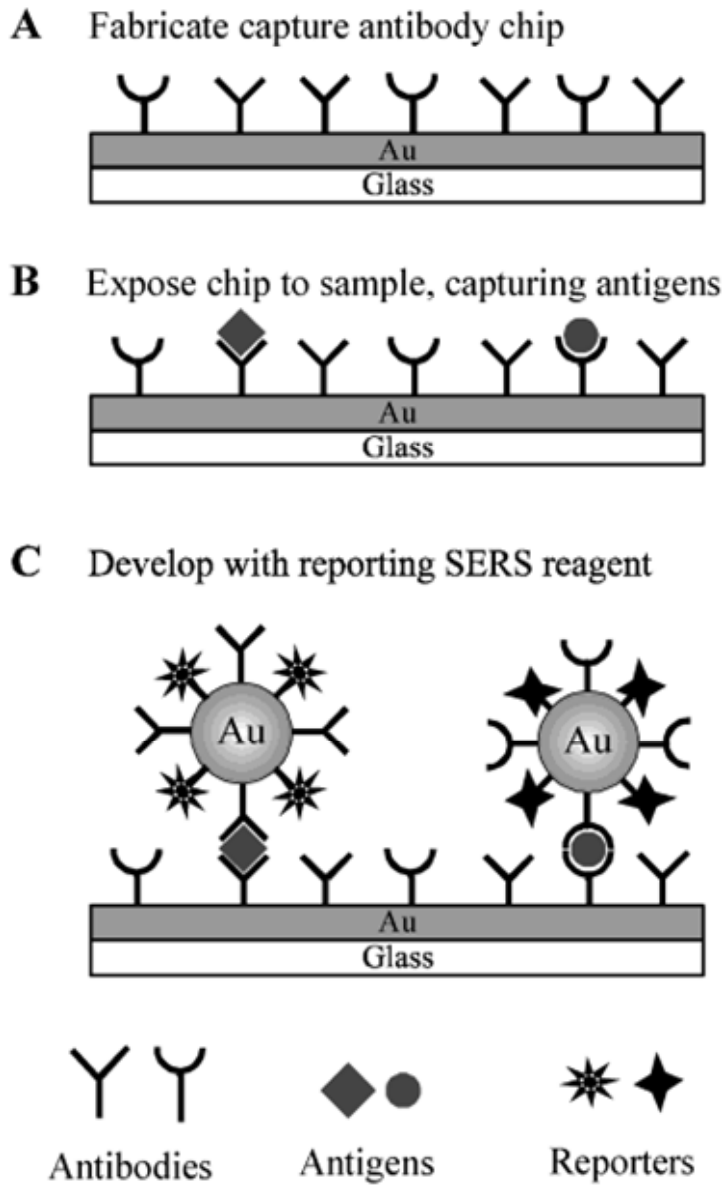

Figure 3. Gold chip-based immunoassay using antibody conjugated Au NPs as SERS nanoprobes

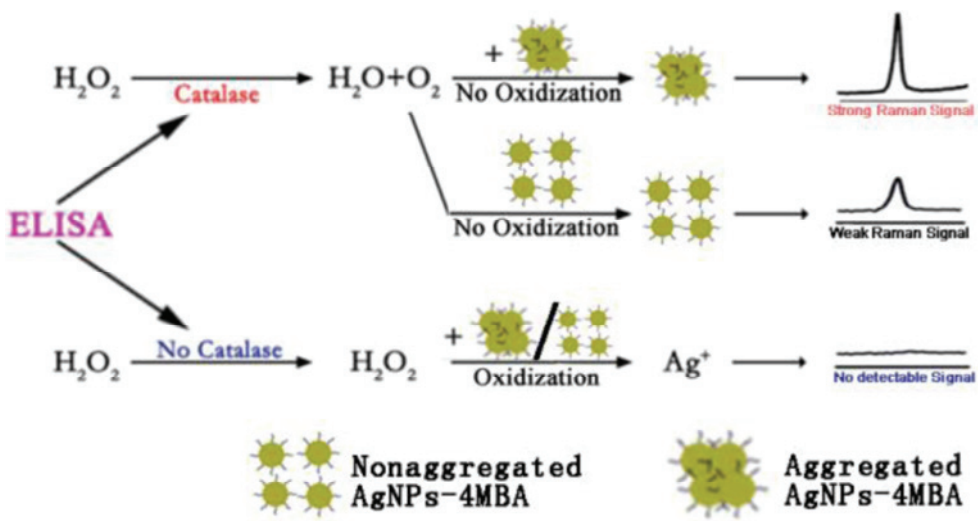

Figure 4. SERS enzime-linked immunosorbent assay using aggregated silver NPs.[64]

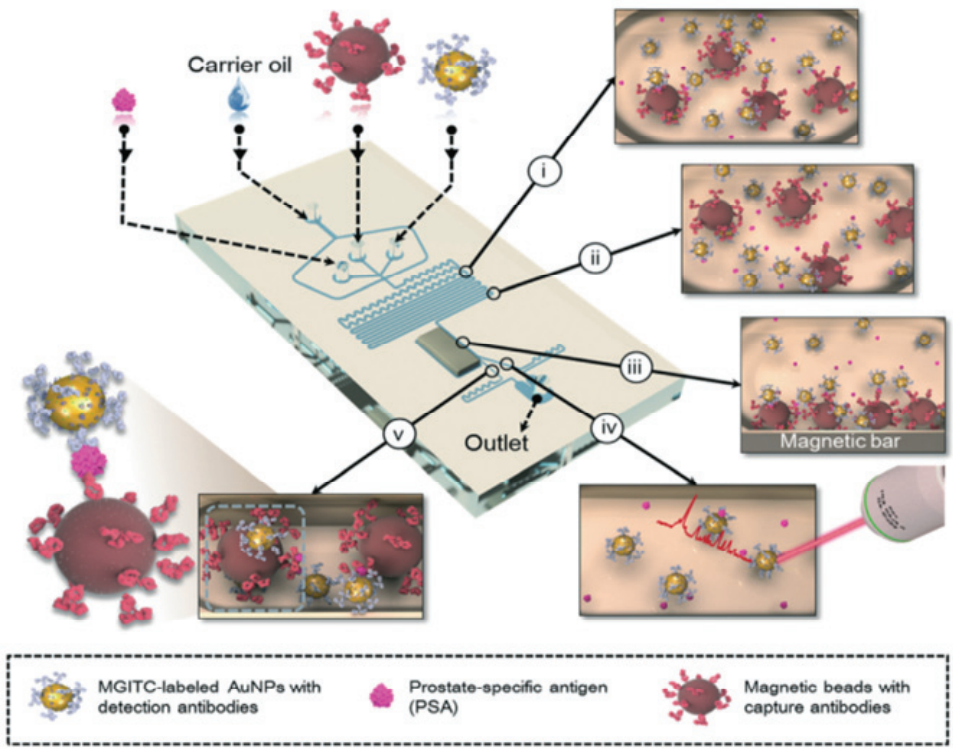

Figure 5. Droplet microfluidics-based immunoassay using magnetic beads and Au NPs.[67]

3. 2. *In vivo* application of SERS nanoprobes

Since the first application of SERS using PEGylated gold nanospheres for *in vivo* tumor targeting in 2008,[29] related researches have been heavily performed. Potent of multiplexed imaging in mice also demonstrated. Because few types of NIR fluorescent agent for in vivo imaging exist, and the spectral overlap matters in detection of multiple targets, Raman imaging has attracted much attentions as a powerful method to overcome several limitations of other imaging tools.

Lee and co-workers reported Au/Ag hollow-shell assemblies on the surface of silica nanospheres (NIR SERS dots), and the signals were detected effectively from deep tissues of up to 8 mm depth exhibiting a capability for use in an *in vivo* multiplex detection (Figure 6a).[18] Gambhir and co-workers simultaneously injected the five SERS nanoparticles intravenously to image their natural accumulation in the liver (Figure 6b), demonstrating the linearly correlation of Raman signal with SERS concentration after injecting four spectrally unique SERS nanoparticles.[76] And thereafter they also reported a brain tumor imaging using a triple-modality MRI-photoacoustic-Raman nanoparticle.[77]

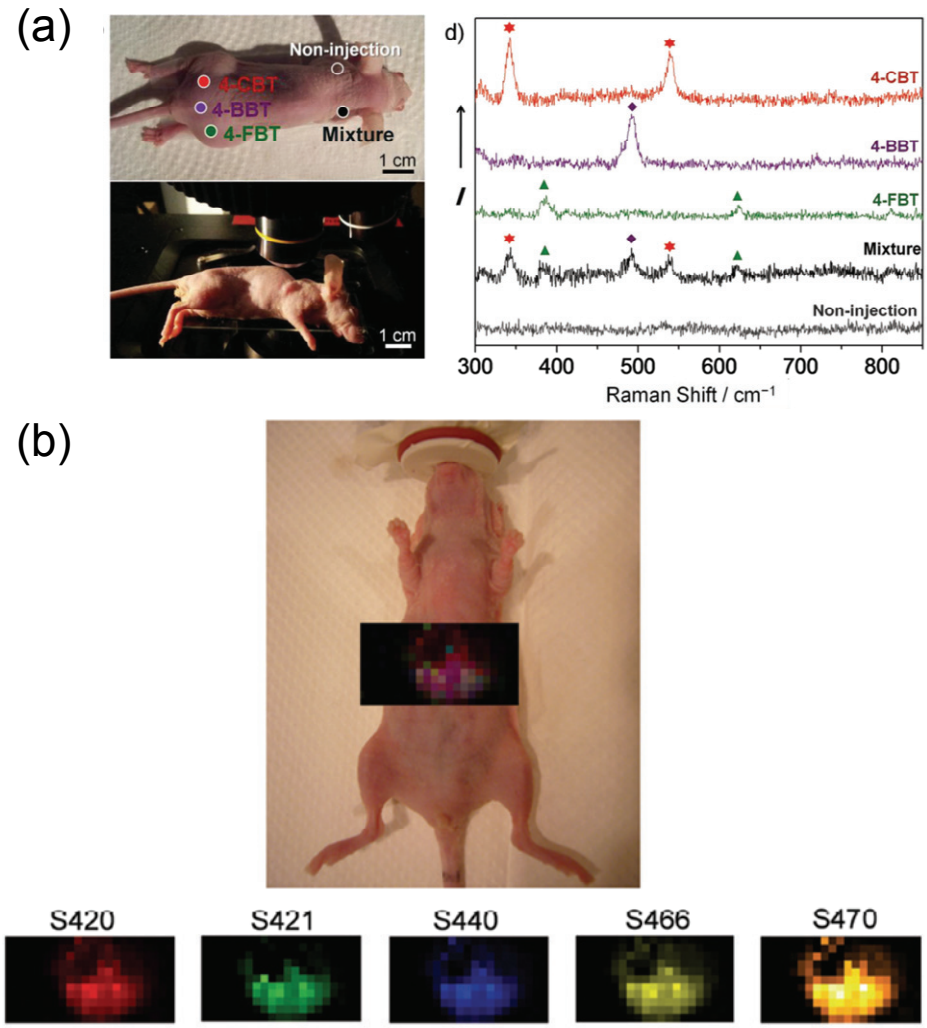

Figure 6. In vivo application of SERS nanoprobes for multiplexed detections.

(a) SERS spectra from NIR SERS dots injected inside the mouse, and (b) Raman image of liver overlaid on digital photo of mouse, showing accumulation of all five SERS batches accumulating in the liver after 24 h post i.v. injection.

4. Research Objectives

While several studies on SERS-based immunoassay with excellent sensitivity have been reported, most of these studies paid little attention to reproducibility explicitly. For practical application, reproducibility is considered as important as sensitivity. Hence, the objective of this research was development of reliable and reproducible immunoassay platform with broad dynamic ranges, and the three aspects are considered as key strategies. The first one is the reproducibility of nanoprobes in SERS intensity. The second one is readout reliability that is required in Raman signal collection from sub-millimeter area. The third one is the reproducibility of overall immunoassay which can be expressed in standard deviation for each concentration and for all concentration. We designed our immunoassay platforms considering all these aspects which ultimately have led to the improved reproducibility and discussed as follows.

In chaper I, a sensitive hetero-nanostructure was demonstrated as a SERS nanoprobe which has a strong and highly uniform SERS activity. Firstly, it was demonstrated that the SERS dot, which is the fabrication

and sensitivity of the SERS probe has been well-established, exhibited homogeneous signal intensity with single-particle detection sensitivity and high photostability during prolonged exposure. Secondly, a SERS nanoprobe which consists of an Ag shell and Au NP satellites (Ag-Au SS) was developed. The plasmonic resonance of Ag-Au SS is red-shifted to the NIR region with additional enhancements compared to the silver bumpy nanoshell structure, enabling the detection even at a single probe level. The Ag-Au SS probe is 100% detectable under 785-nm photoexcitation due to multiple SERS hot spots which were designed to generate reproducible and isotropic SERS activity.

In Chapter II, a fast and reliable readout method for quantitative analysis of SERS nanoprobes (SERS dot) on chip surface was studied. The complete survey scan and the sampled spot scanning method were compared to reveal the heterogeneous effect of SERS nanoprobe on quantitative bio-assays. And a practical and reliable readout strategy was proposed for chip-based immunoassays using SERS. This could give an insight to overcome the problems of current Raman readout methods.

In chapter III, we developed a SERS-based immunoassay (SIA) platform with high sensitivity and a wide dynamic range for PSA detection. The SERS dots and conventional glass slides with spot-arrays

were used as probes and capture substrates respectively. Combination of the rapid and full-area reading method[78] with SERS probes resulted in PSA detection with a large dynamic range (0.001−1000 ng/mL) and low limit of detection (0.11 pg/mL) compared with those of commercially available immuno-radiometric assay (IRMA) and chemiluminescence immunoassay (CLIA) kits. Furthermore, the developed SIA was successfully applied to detect the PSA in a patient's serum, showing the potentials for practical application in clinical field.

Chapter I. SERS Nanoprobes for Multiplexed and Quantitative Biological Application

1. Experimental section

1. 1. Materials

Tetraethylorthosilicate (TEOS), 3-mercaptopropyltrimethoxysilane (MPTS), ethylene glycol (EG), poly(vinyl pyrrolidone) (PVP, Mw ~40,000), silver nitrate ($AgNO_3$, 99.99%), octylamine (OA), tetrachloroaurate trihydrate ($HAuCl_4 \cdot 3H_2O$, 99.9%), trisodium citrate, cysteamine, (3-aminopropyl) triethoxysilane (APTES), phosphate buffered saline (PBS, pH 7.4), 4-bromobenzenthiol (4-BBT), 4-chlorobenzenthiol (4-CBT) and 4-fluoro-benzenthiol (4-FBT) were purchased from Sigma-Aldrich and used without further purification. Ammonium hydroxide (NH_4OH, 27%), and 2-propanol (99%) were purchased from Daejung (Siheung, Korea). Ethanol of high purity (99.8%) was purchased from Carlo Erba (Milano, Italy). Methoxy poly(ethyleneglycol) sulfhydryl (mPEG-SH) (Mw 2,000) was purchased from Sunbio (Anyang, Korea).

1. 2. Preparation of SERS dots

SERS tags, called SERS dots in this study, were prepared as the previously reported method with slight modifications for this study.[79] Briefly, silica nanoparticles (Si NPs) with a diameter of *ca.* 170 nm were prepared by the

Stöber method,[80] and then, functionalized with thiol groups by MPTS treatment. The Ag NPs (*ca.* 10 nm) were introduced on the surface of the thiol-functionalized silica sphere by the amine-assisted growth method.[81] Then, a 1-mL aliquot of 5-mM Raman label compound (RLC; 4-FBT and 4-CBT, in ethanol) was added to 5 mg of the Ag-coated Si NPs. The resulting dispersion was shaken for 1 h at 25 °C. The RLC-coded Ag-coated Si NPs were centrifuged and washed with ethanol twice. To encapsulate the Ag-coated Si NPs with a silica shell, the NPs were dispersed in 15 mL of dilute sodium silicate aqueous solution (0.036 *wt*% SiO_2). The dispersion was stirred with a magnetic stirrer for 12 h at room temperature. Finally, 60 mL of ethanol, 250 μL of aqueous NH_4OH (27%) and 30 μL of TEOS were added to the reaction mixture, and stirred for 24 h at room temperature. The resulting SERS dots were centrifuged and washed with ethanol several times.

1. 3. Preparation of bumpy Ag shell

Tetraethylorthosilicate (TEOS, 1.6 mL) was dissolved in 40 mL of ethanol, followed by the addition of 3 mL of aqueous ammonium hydroxide (27%). The mixture was vigorously stirred for 20 h at 25 ^oC. The synthesized silica nanoparticles (NPs) were centrifuged and then redispersed in ethanol

several times to remove the excess reagents. These silica NPs were then dispersed in 6 mL of ethanol containing 300 μL of MPTS and 60 μL of aqueous ammonium hydroxide (27%) for functionalization with the thiol group. The mixture was stirred using a magnetic stirrer for 12 h at 25 ^{o}C. The resulting MPTS-treated silica NPs were centrifuged and washed with ethanol several times for purification. Five milli-gram of PVP was mixed with 25 mL of ethylene glycol, followed by the addition of 3 mg of MPTS-treated silica NPs. Then, 25 mL of $AgNO_3$ solution (7 mM, in ethylene glycol) was added to the silica NP suspension and thoroughly mixed (final concentration of $AgNO_3$ was 3.5 mM), followed by the rapid addition of 41.3 μL octylamine into the above solution (final concentration of octylamine was 5 mM). The resulting dispersion was stirred for 1 h at 25 ^{o}C. The particles were subsequently centrifuged and washed with ethanol several times for purification.

1. 4. Preparation of gold nanoparticles

Fifty milli-gram of $HAuCl_4$ was dissolved in DI water (50 mL) followed by the addition of 1 mL of citrate aqueous solution (1%, w/w). The temperature during the reaction was maintained at 100 °C for 30 minutes and the colloidal solution was then kept at room temperature for 24 h

while stirring. The resulting Au NPs stock solution was stored at 4 °C. Before use, the Au NPs solution was transferred to an ethanol solvent.

1. 5. Preparation of amine-functionalized silicon wafer

Silicon wafers were ultra-sonicated for 15 minutes in acetone and in DI water sequentially to clean the surface. The surface of the silicon wafer was then activated by soaking in a piranha solution (a mixture of H_2SO_4 and 30% H_2O_2 (3:1, v/v)) for 15 minutes, rinsed with DI water several times, and then dried by blowing with nitrogen gas. The self-assembled monolayer (SAM) was formed by dipping the cleaned silicon wafer into a 5 v/v% solution of APTES solution (5% in anhydrous ethanol, v/v) for 30 minutes. The APTES-treated silicon wafer was sonicated in ethanol for 2 minutes to remove excess chemicals. After sonication, the APTES-treated silicon wafer was rinsed with ethanol and deionized (DI) water several times and then dried by blowing with nitrogen gas.

1. 5. Fabrication of Ag-Au Shell-Satellite (Ag-Au SS) particle

For immobilization of the Ag shell particles, amine-functionalized silicon wafer was immersed in an Ag shell colloidal solution for 3 h. After adsorption of the Ag shell on the silicon wafer, Raman label compound

(RLC) (4 mM in ethanol) and cysteamine (2 mM in ethanol) as a linker molecule were co-adsorbed on the surface of the Ag shell by dipping the silicon wafer in RLC and cysteamine mixture solution for 1 h. The silicon wafer was then briefly rinsed with ethanol. Then, the silicon wafer was immersed in the Au NPs solution (*ca.* 19 nm in diameter, 20 nM in ethanol) for 2 h. The silicon wafer with Ag-Au SS particles was sonicated in ethanol for 1 minute, so that the resulting Ag-Au SS particles could be detached selectively from the silicon wafer and placed into the ethanol.

1. 6. Single-Particle SERS measurement

For single particle SERS measurement, the Raman compound labeled Ag-Au SS suspension (0.1 mg mL^{-1} in ethanol) and the SERS dot dispersion (0.1 mg mL^{-1} in ethanol) was dropped and dried on a patterned slide glass, and SERS spectra were measured by point-by-point mapping with 1-μm step size. The mapping experiments were carried out using a ×100 objective lens (NA 0.90). After the SERS measurement, SEM images of the same area were obtained using field emission-scanning electron microscopy (JSM-6701F, JEOL, Tokyo, Japan) for single particle based analysis.

1. 7. Calculation of the SERS enhancement factor

SERS enhancement factors (EF) for the Ag shells and Ag-Au SS probes can be calculated using the following equation:

$$EF = (I_{SERS} \times N_{normal})/(I_{normal} \times N_{SERS}) \qquad \text{(eq. 1)},$$

where I_{SERS} and I_{normal} are the intensities of the bands from SERS and normal Raman scattering, and N_{normal} and N_{SERS} are the numbers of RLC (4-FBT was used in this experiment) in pure form and self-assembled on the probe surface. The Raman band at 1075 cm^{-1} for 4-FBT was used to estimate the EF. Raman signal intensities were measured for both single particles and neat 4-FBT using identical laser power (28 μW) for the EF calculation. Probing volume (18.8 μm^3) was approximated as a cylinder form with a diameter of 2 μm and a height of 6 μm for the normal Raman measurements. The molecular weight and density of 4-FBT are 125.19 g/mol and 1.203 g/cm^3, respectively, thus N_{normal} was estimated 1.1×10^{11}. N_{SERS} was calculated by geometrically estimating the particle's surface area (Ag shell is assumed complete spherical shape, r = 125 nm) and a molecular footprint of 4-FBT (0.383 nm^2/molecule),[82] assuming that the only 4-FBT molecules were covered on surface of Ag shell to avoid overestimation of EF calculation. Thus, N_{SERS} of Ag shell and Ag-Au SS was approximately 2.05×10^5.

1. 9. Bio-application of Ag-Au SS probes

For *in vivo* application, Ag-Au SS probe was PEGylated by mPEG-SH (Mw 2,000) to improve their biocompatibility. The 4-FBT-coded Ag-Au SS was incubated in a 1-mL of mPEG-SH solution (2 mM in ethanol) for 1 h, followed by centrifugation and suspension in fresh PBS buffer (pH 7.4) several times. A male nude mouse was anesthetized with an intraperitoneal injection of ketamine and xylazine mixture solution. The PEGylated Ag-Au SS dispersion was injected subcutaneously into the gluteal region of the mouse. SERS spectra were obtained from each injection depth (*ca*. 3 mm) using a Raman system with a 785-nm photoexcitation. This study was approved by Seoul National University Bundang Hospital Institutional Animal Care and Use Committee (IACUC No. BA1306-131/052-02).

2. Results and Discussion

2. 1. Synthesis and characterization of SERS dots

As illustrated in Figure 1-1a, SERS dots consist of Raman label compound (RLC)-coated silver nanoparticles (Ag NPs) assembled on a silica core (*ca.* 170 nm). Ag NP-assembled silica (Figure 1-1bi) is further encapsulated in an outer silica shell (Figure 1-1bii) to prevent aggregation and facilitating further surface modification. First, the optical properties of SERS dots were evaluated. To assess sensitivity, single-particle SERS measurements were performed by point-by-point mapping on 4-chlorobenzenthiol-labeled SERS dot (SERS dot$_{4\text{-CBT}}$)-dispersed glass slides with photoexcitation at 532 nm. Subsequently, scanning electron microscopy (SEM) images were compared with the corresponding SERS intensity maps to verify the locations of single particles.

Figure 1-2a shows a typical SERS spectrum of a single SERS dot$_{4\text{-CBT}}$ obtained using 580-μW sample power and 3-s acquisition. SERS intensity map for the 1568 cm^{-1} Raman band of the SERS dots$_{4\text{-CBT}}$ dispersed on a glass slide is overlaid with the corresponding SEM image (Figure 1-2b). The Raman intensity map showed that the intensities of SERS dots were sufficient for detection of single particles. Twenty-four of total 29 SERS

dot$_{4\text{-CBT}}$ particles (82%) exhibited single-particle SERS activity under our experimental conditions, and the signal fluctuations were within one order of magnitude (Figure 1-2c). These strong and uniform intensities of SERS signals are due to the ensemble averaged signal effect[18,83-86] of Ag NP-assembled structures. In addition, a photostability test of a single SERS dot$_{4\text{-CBT}}$ particle was performed using laser irradiation (580 μW) for 100 s. Each spectrum was obtained consecutively with 10 s acquisition time (Figure 1-2d). The SERS intensity decreased by only 25% and reached a plateau after 80-s irradiation. These results indicate that SERS dots are sufficiently sensitive for single particle detection with little particle-to-particle variation and photostability for quantitative immunoassay. Thus no additional signal enhancement, such as plasmonic coupling between probe particles and the gold substrate,[73] is necessary. The use of self-bright particles as probes reduces the heterogeneity of Raman intensity in SERS-based immunoassays, and simplifies the assay protocol.

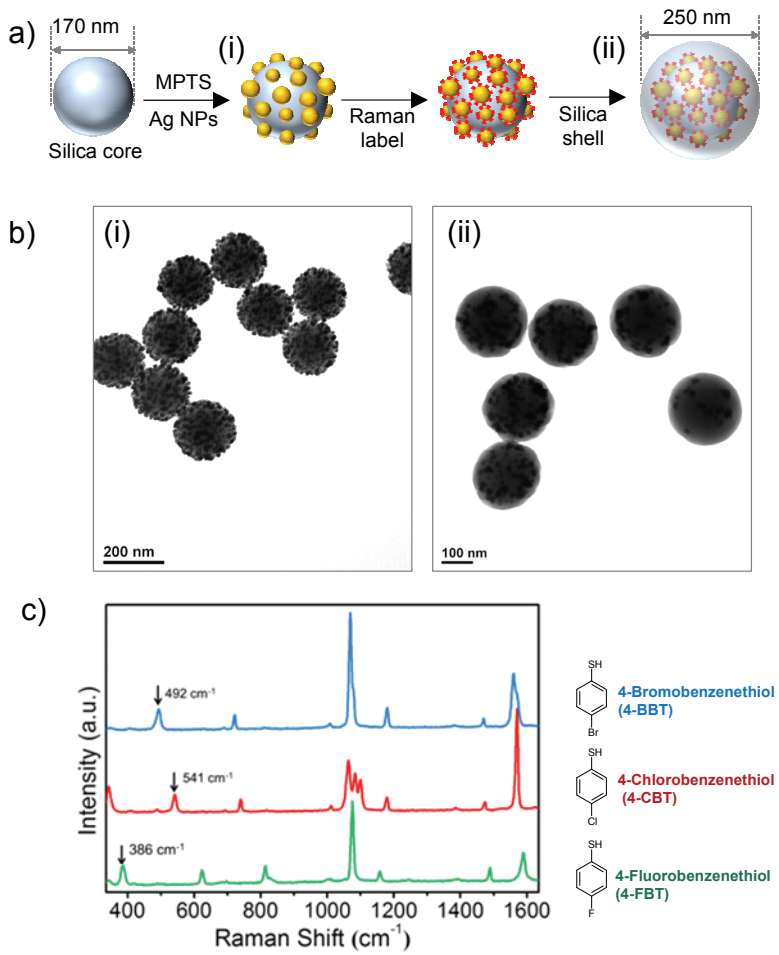

Figure 1-1. Schematic representation of SERS dots and their recorded Raman spectra.

(a) Silver nanoparticles-assembled silica core with a 180-nm diameter are labeled with a Raman active material, and then, silica coating to yield a particle of 250-nm diameter. (b) TEM images of (i) Ag NPs-assembled Silica NPs and (ii) SERS dots (c) The unique SERS spectra of the molecular vibrations in the different Raman label compound with photoexcitation at 532 nm.

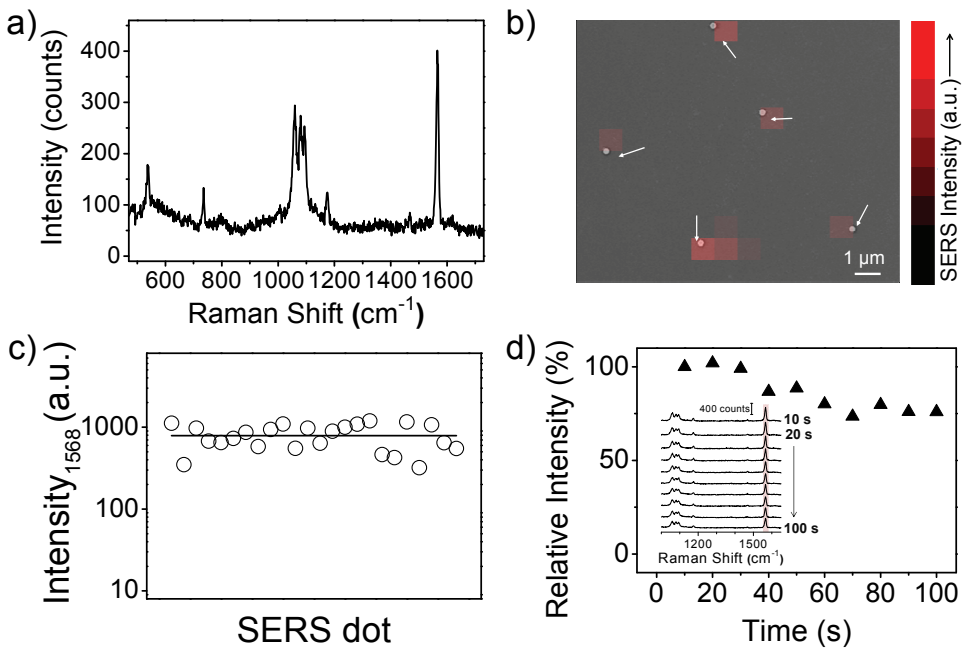

Figure 1-2. Characterization of a single SERS dot particle.

(a) Typical SERS spectrum of a single SERS dot4-CBT particle on a slide glass. The spectrum was obtained using 532 nm photoexcitation (0.58 mW at the sample) and a 3 s acquisition time. (b) SERS intensity map overlaid with the corresponding SEM image. Arrows indicate single SERS dot particles located in signal-detected regions. (c) SERS intensity distributions of the 1568 cm^{-1} band obtained from single SERS dot4-CBT particles (N=24). Y-axis has a log scale. (d) Photostability of a single SERS dot. SERS intensity changes (relative to the initial value) obtained from a single SERS dot with continuous laser exposure (100 s). Inset, spectra obtained using 532 nm photoexcitation of 0.58 mW at the sample and a 10 s acquisition time.

2. 2. Synthesis of Ag-Au SS probes

Fabrication details of Ag-Au SS probes are illustrated in Figure 1-3. We utilized a solid support and selective desorption method[36] to prevent NPs' aggregations during synthesis and for easy separation of assembled nanoparticles and non-assembled nanoparticles. First, amine-functionalized silicon wafer was immersed into the Ag shell colloidal solution for 3 h (Figure 1-3a). The Ag shell (251 ± 16 nm in diameter, *ca.* 50 nm of shell thickness) was synthesized by using a one-step method.[17] It has dielectric silica core and broad range surface plasmonic bands. The Ag shell facilitates the development of the NIR-active probes owing to the intrinsic SERS activity of the Ag shell in the NIR region. After the attachment of Ag shells on the silicon wafer, a Raman label compound (RLC) (4 mM in ethanol) and cysteamine (2 mM in ethanol) as a linker molecule were co-adsorbed on the surface of the Ag shell by dipping the silicon wafer in RLC and cysteamine mixed solution for 1 h (Figure 1-3b). Cysteamine is a well-known cross-linker molecule which can provide structural stability of nanoassemblies by forming a monolayer on the metal surface via chemisorption with the thiol group, and attaching another substances with the amine group. [87] Next, the citrate-capped Au NPs (*ca.* 20 nm) were immobilized on the surface of the amine functionalized Ag

shell and silicon wafer (Figure 1-3c). Finally, the Ag-Au SS probe adsorbed silicon wafer was sonicated in ethanol for 1 minute, leading to the selective detachment of Ag-Au SS probes from the silicon wafer into the ethanol because of the different desorption efficiency depending on the particle size (Figure 1-3d, and Figure 1-4).[36]

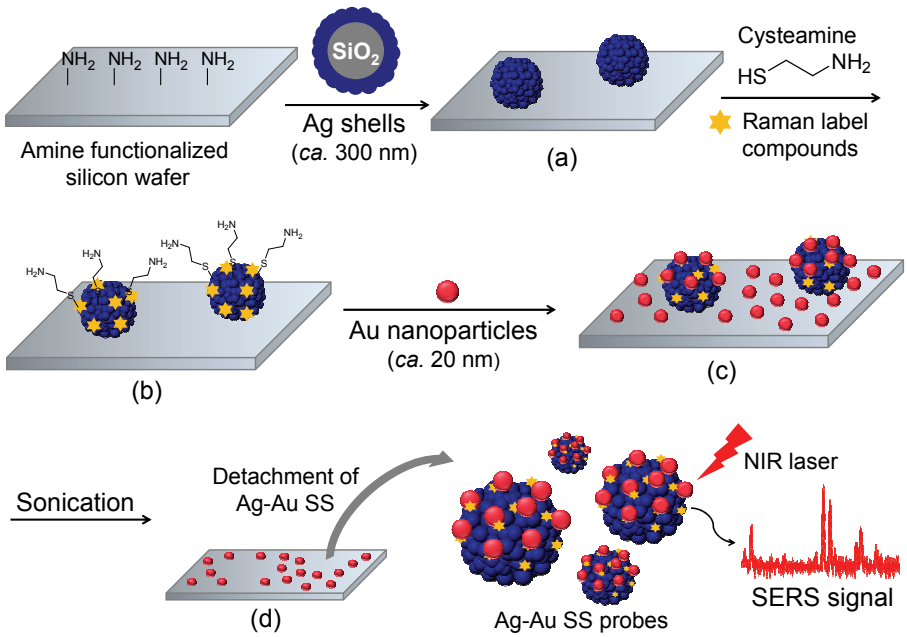

Figure 1-3. Schematic illustration for the fabrication of Ag shell-Au satellite (Ag-Au SS) probes on solid substrate.

(a) Ag shells are immobilized on the amine-functionalized silicon wafer through electrostatic interactions. (b) Cysteamine (a linker molecule) and Raman label compound are adsorbed on the surface of Ag shells. (c) Au NPs as satellites were introduced electrostatically onto Ag shells on a silicon wafer. (d) Ag-Au SS probes were selectively detached from the silicon wafer by moderate sonication.

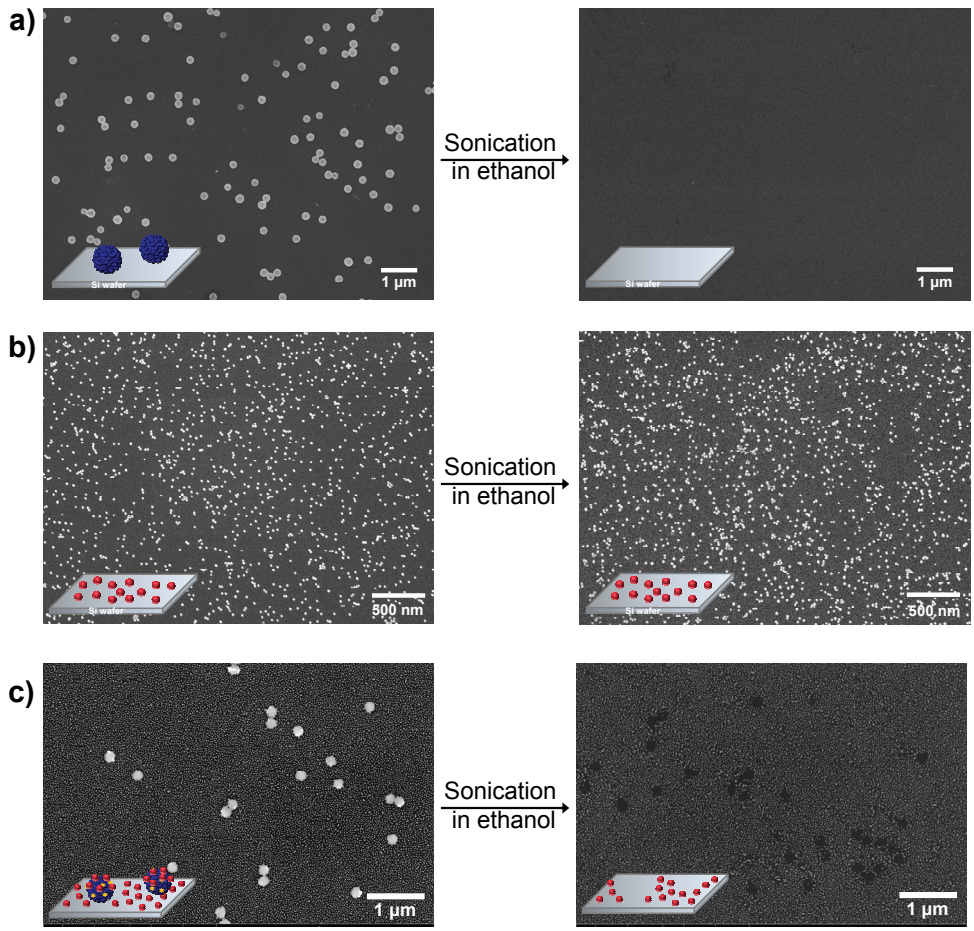

Figure 1-4. Comparison of detachment efficiencies of Ag shell and Au NP from the silicon wafer into ethanol medium.

(a) SEM images of Ag shell-attached silicon wafer before (left) and after (right) sonication. (b) SEM images of Au NPs-attached silicon wafer before (left) and after (right) sonication. (c) SEM images of Ag-Au SS-fabricated silicon wafer before (left) and after (right) sonication.

2. 3. Structural Analysis

The samples during the fabrication process were characterized by scanning electron microscopy (SEM), transmission electron microscopy (TEM), and energy dispersive X-ray spectroscopy (EDX) measurements. Before detachment of the Ag-Au SS probes from the silicon wafer, the formation of Ag shell-Au satellite structures was confirmed by SEM (Figure 1-5a) and EDX analysis (Figure 1-5b-e). From the SEM image, it was confirmed that Au NPs were successfully immobilized on the surface of Ag shells as well as on that of the silicon wafer. The number of Au satellite NPs per Ag shell was estimated to be 21 ± 4 on average by counting the Au satellite NPs on the observable side from 60 Ag-Au SS probe particles. In addition, the elemental mapping images clearly show that both the Ag atoms and the Au atoms are well distributed throughout the core part, indicating that the Ag-Au heterometallic structure was successfully assembled.

Next, the morphology and optical properties of the detached Ag-Au SS probes were confirmed. The Au NPs existing on the surface of the Ag shell were clearly observed as shown in Figure 1-6b (red arrows indicate satellite Au NPs), compared with the TEM image of the Ag shell (Figure 1-6a). This result proves that the Ag-Au SS structure is maintained during the detachment process. Furthermore, the UV-Vis-NIR extinction spectra

of Ag-Au SS probes (λ_{max} = 698 nm) demonstrate that their surface plasmon band was red-shifted from that of the individual Ag shell (λ_{max} = 620 nm) and Au NPs (λ_{max} = 520 nm) (Figure 1-7). This red-shifted plasmon resonance band is attributed to the strong plasmon coupling between the Ag shell and Au NPs (less than 1 nm gap, Figure 1-6c),[88] affording Ag-Au SS probes a plasmon coupling band in the NIR region.

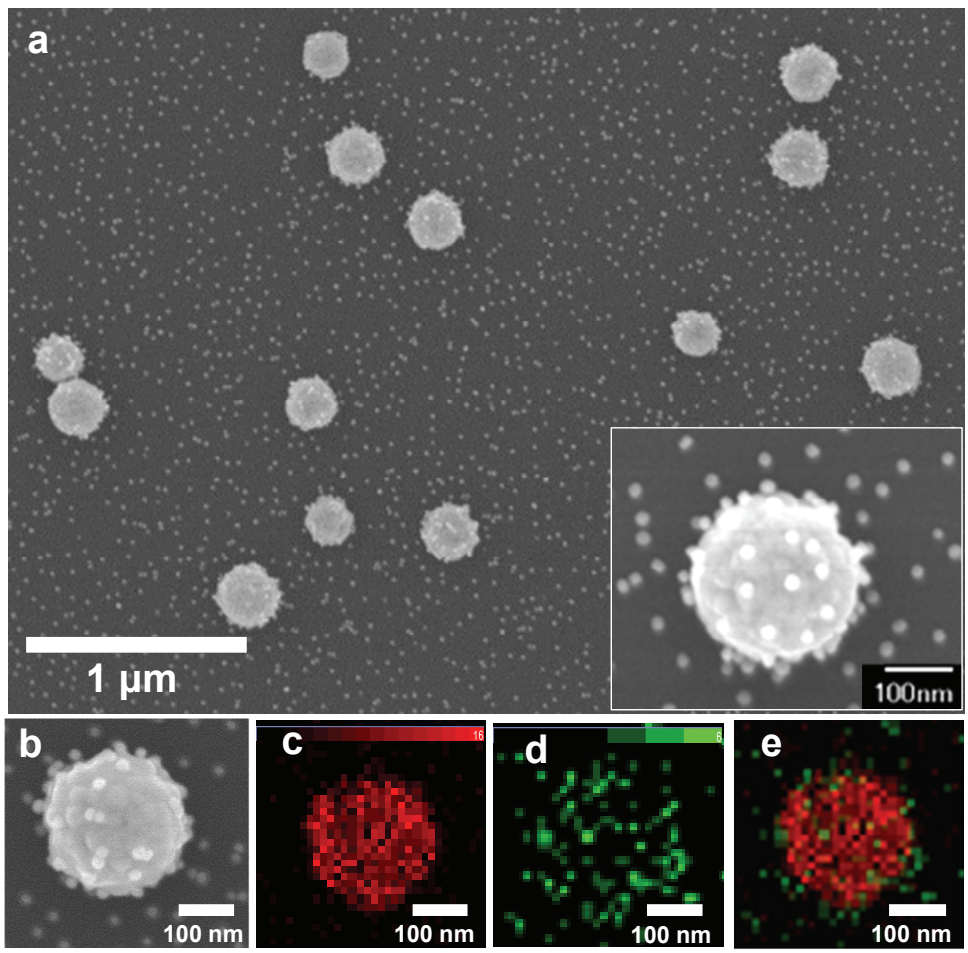

Figure 1-5. Structural and optical characteristics of Ag-Au SS probes.

(a) SEM image of the Ag-Au SS probes fabricated on a silicon wafer. (b) Highly magnified SEM image of one Ag-Au SS probe and its EDX maps showing the elemental distributions of (c) Ag from L_{α}, (d) Au from M_{α}, and (e) merged image of Ag and Au.

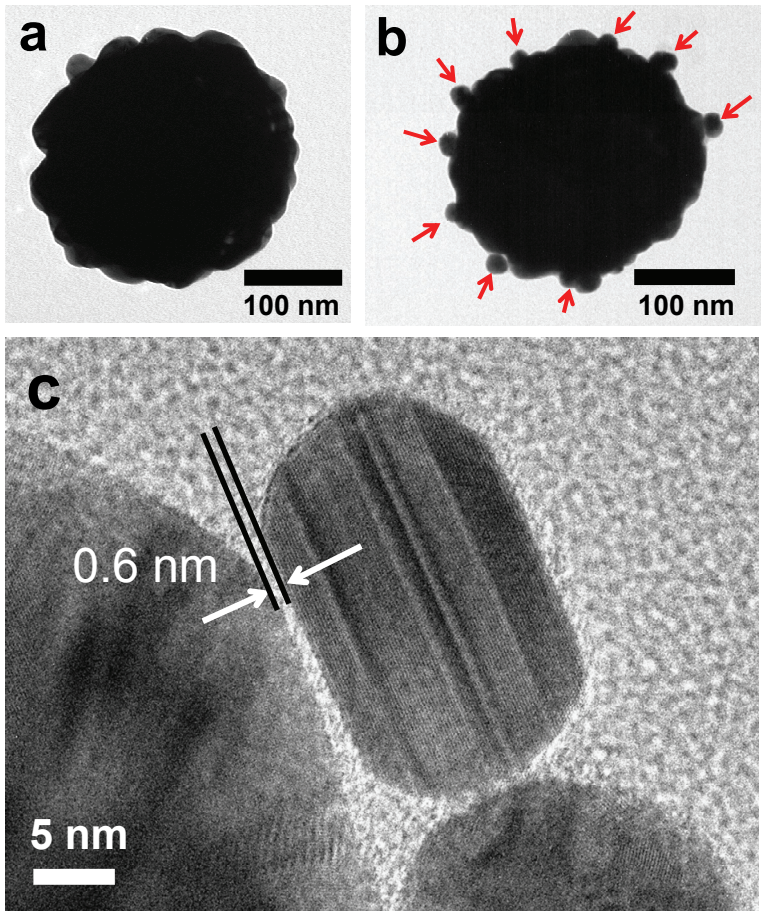

Figure 1-6. TEM images.

(a) Ag shell, and (b) Ag-Au SS probe. (c) HR-TEM image of Ag shell-to-Au satellite interparticle gap. The two arrows indicate the sub-nanometer gap.

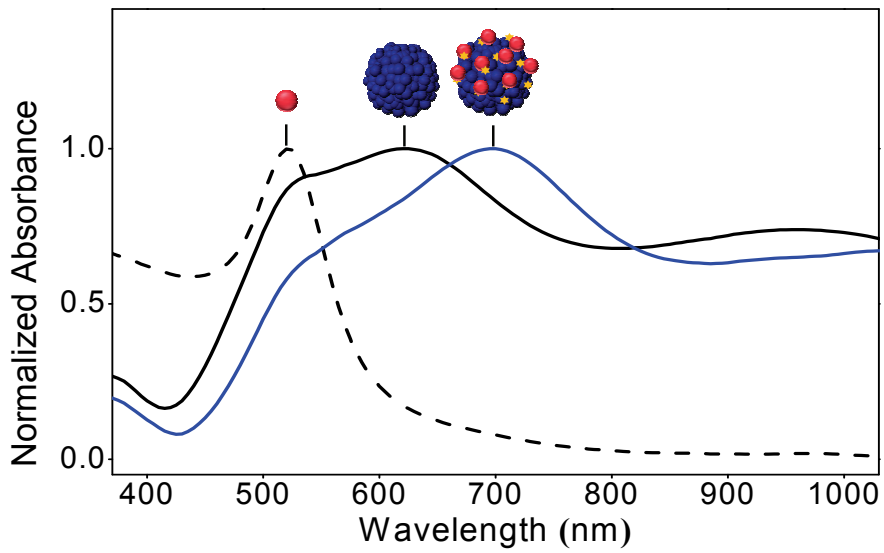

Figure 1-7. UV-Visible-NIR extinction spectra

Spectrum of Au NPs (black dashed line, λ_{max} = 520 nm), Ag shells (black solid line, λ_{max} = 620 nm), and Ag-Au SS probes (blue solid line, λ_{max} = 698 nm).

2. 4. Single-Particle Activity of Au-Ag SS

To evaluate the Ag-Au SS probe as the NIR sensitive SERS probe, the SERS spectra of single probes were obtained with three different excitation lines (532, 647, and 785 nm). Raman measurements were performed by point-by-point mapping with a 1-μm step size under the appropriate condition depending on the excitation wavelengths. Subsequently, SEM images were compared with the corresponding Raman maps to ensure the existence of single particles. Figure 1-8a shows typical SERS spectrum of an Ag-Au SS probe coded with 4-fluorobenzenethiol obtained by 785-nm photoexcitation (28 μW) and 10-s acquisition. SERS intensity map of the 1075-cm^{-1} band from Ag-Au SS probes dispersed on silicon wafer is drawn overlayed with its corresponding SEM image (Figure 1-8b). SERS enhancement factors (EFs) and percentages of detectable single particles for three different excitation lines were estimated for the Ag-Au SS probe and for the Ag shell as comparison (Figure 1-8c, 1-9 and Table 1-1).

Interestingly, two notable features were found from this result. First, the SERS EF values of Ag-Au SS exhibit 4.1-fold (532 nm), 3.1-fold (647 nm), and 2.5-fold (785 nm) increase compared with those of Ag shells. Especially, the Ag-Au SS exhibited the highest EF value (1.4×10^6 on average) for NIR excitation (785 nm) among the three laser lines.

Although the bumpy surface of the Ag shell induces an electromagnetic field enhancement, the inter-particle gaps in the shell-satellite structure can provide further enhancement, producing a highly concentrated electromagnetic field.[52] As hot spots were generated between the particles, the SERS intensities of Ag-Au SS probes were distributed more broadly compared to the intensities of Ag shells under photoexcitation of 532 nm and 647 nm. However, in case of 785 nm photoexcitation, the relative signal distribution of Ag-Au SS was decreased compared to one of Ag shell. The difference of such trends is expected to be resulted in the different enhancement processes; the locally enhanced field between the hotspots contributed to the enhancement under 532 nm and 647 nm excitations, however, in case of 785 nm excitation, the red-shifted plasmon resonance of Ag-Au SS had contribution to enhanced signals. Secondly, the detectability of Ag-Au SS probes was increased remarkably compared with that of the Ag shell, reaching up to 100% in the case of NIR excitation (785 nm). In addition, the distributions of EF values from the Ag-Au SS probes were highly uniform, which is attributed to the multiple hot spots produced by shell-satellites structure. This feature refers to ‘reproducibility’ of SERS intensity over probe particles, of which

concept follows the previously reported article showing the degree of the particle-to-particle signal distribution.[13]

Another aspect is 'reproducibility' of SERS intensity irrespective of incident laser polarization. To confirm whether or not the signal uniformity of Ag-Au SS is isotropic over incident laser polarization, SERS spectra of an Ag-Au SS probe were obtained using a 785-nm laser, of which the polarization was rotated in three directions. As shown in Figure 4, the 4-FBT signals of the Ag-Au SS probe were consistent when the laser polarization was rotated by 45° and 90° away from the onset axis. This feature is superior to the dimer structures, of which the SERS signals have vanished when the excitation laser is polarized orthogonal to the longitudinal axis.[46,89] In addition, the photostability of Ag-Au SS probes was tested over time for proving the reproducibility. We obtained the SERS spectra from the single Ag-Au SS particle while irradiating laser lights for approximately 100 s. Each spectrum was obtained with 5-s acquisition (Figure 1-10a). The signal intensities exhibited little decrease indicating that Au-Ag SS probe is stable under laser exposure (Figure 1-10b). These results reveal that the Ag-Au SS probes are a robust platform for highly reproducible SERS analysis due to the multiple hot spots and the red-shifted plasmonic resonance.

In order to expand the utility of Ag-Au SS probe, two types of Ag-Au SS were prepared by using different RLCs such as 4-chlorobenzenethiol (4-CBT), and 4-bromobenzenethiol (4-BBT). Each type of Ag-Au SS has distinctive spectral fingerprint and exhibits strong single-particle SERS activities, suggesting that these Ag-Au SS probes can be used in multiplexed analysis (Figure 1-11).

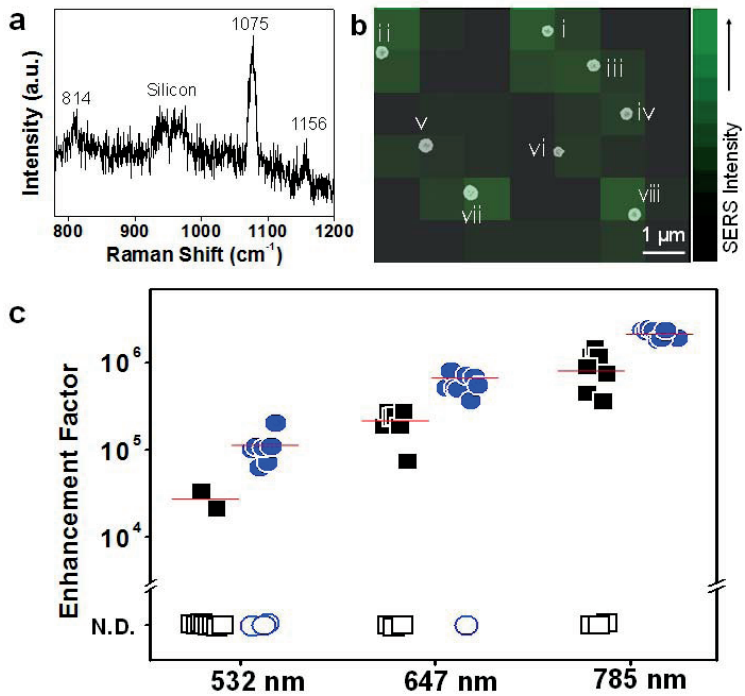

Figure 1-8. Analysis of SERS enhancement of Ag-Au SS probes by single probe particle characterization.

(a) Representative SERS spectrum of an Ag-Au SS probe coded with 4-fluorobenzenethiol obtained by 785-nm photoexcitation (28 μW) and 10-s acquisition. (b) SERS intensity map of the 1075-cm^{-1} band from Ag-Au SS probes dispersed on silicon wafer. The SERS intensity map was overlaid with its corresponding SEM image. Enhancement factor of each Ag-Au SS probe on the silicon substrate at 785-nm photoexcitation is (i) 1.6×10^6, (ii) 1.5×10^6, (iii) 1.4×10^6, (iv) 1.1×10^6, (v) 1.1×10^6, (vi) 1.0×10^6, (vii) 1.2×10^6, and (viii) 1.5×10^6. (c) Enhancement factors of Ag shells (black solid squares) and Ag-Au SS probes (blue solid circles) at three different excitation wavelengths (532, 647, and 785 nm). All empty dots indicate undetectable particles.

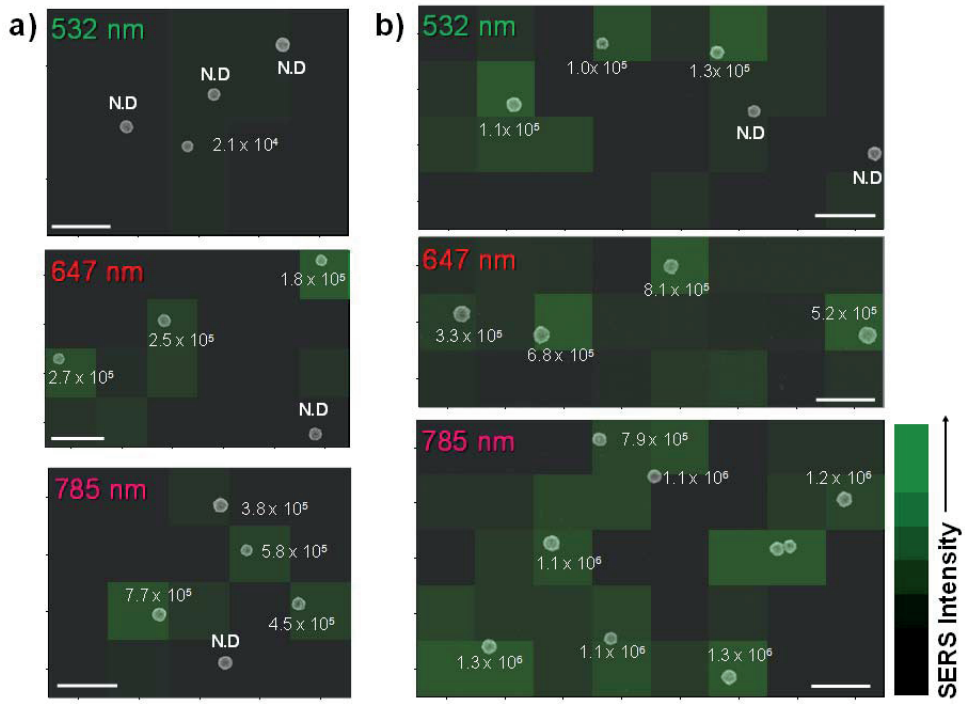

Figure 1-9. Analysis of single particle SERS activity.

SERS intensity maps overlaid with corresponding SEM images for single Ag shell nanoparticles (a) and single Ag-Au SS particles (b) with photoexcitations at 532 nm, 647 nm, and 785 nm. The SERS enhancement factors of each probe are shown. N.D refers to "not detected". Ag shells and Ag-Au SS were coded with 4-FBT. The SERS intensity map for the 532-nm laser excitation was taken under 20 μW at the sample and at 10 s acquisition time, that for the 647-nm laser excitation was taken under 26 μW at the sample and at 2 s acquisition time, and that for the-785 nm laser excitation was taken under 28 μW at the sample and at 10 s acquisition time. All scale bars are 1-μm scale.

Table 1-1. Comparison of single-particle SERS activity between Ag shell and Ag-Au shell-satellite (Ag-Au SS) probes at three excitation wavelengths (532, 647, and 785 nm).

Excitation wavelength	**Ag shell**		**Ag-Au SS**	
	SERS EF value[a]	Detectable single particles (%)	SERS EF value[a]	Detectable single particles (%)
532 nm	**2.7×10^4** ± 23.1%	**20.0**	**1.1×10^5** ± 38.4%	**52.9**
647 nm	**2.1×10^5** ± 31.0%	**50.0**	**6.6×10^5** ± 47.7%	**90.0**
785 nm	**5.7×10^5** ± 42.6%	**66.7**	**1.4×10^6** ± 10.8%	**100.0**

[a]SERS enhancement factor value involving relative standard deviation (RSD); RSD = 100 × (Standard deviation)/(Average)

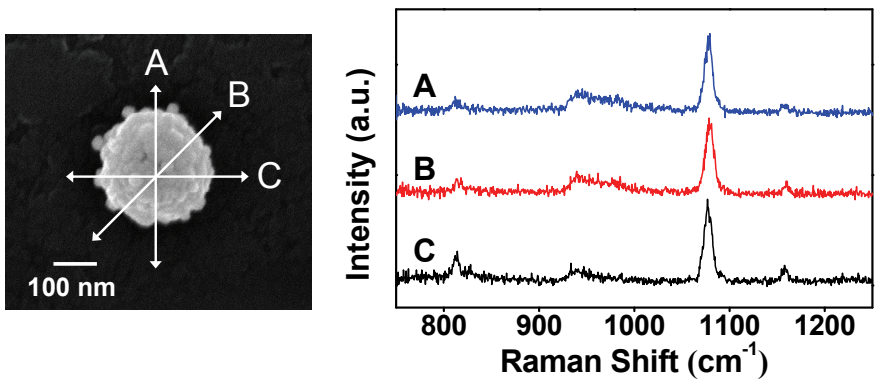

Figure 1-10. SERS spectra obtained from Ag-Au SS probe with different orientations relative to the polarization of the excitation laser.

The 4-FBT signals from the Ag-Au SS probe are consistent when the laser polarizations are rotated by 45° (B) and 90° (C) away from the onset axis (A). All spectra were taken using a 785-nm photoexcitation (180 μW at the sample) and 10 s acquisition time

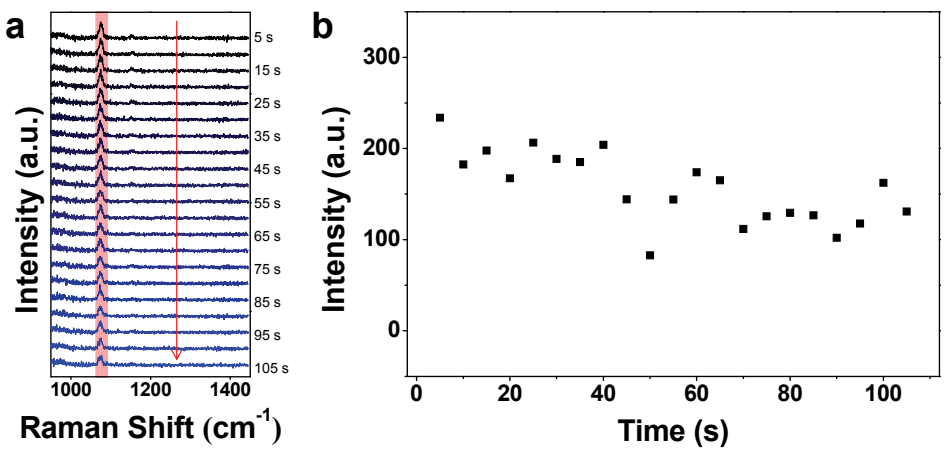

Figure 1-11. Photostability of Ag-Au SS probes with irradiation time.

(a) SERS spectra obtained from single Ag-Au SS probe particle with continuous laser exposure. All spectra were taken with 785-nm photoexcitation of 210 μW at the sample and 5-s acquisition time. (b) SERS intensity of the 1075-cm-1 band over time.

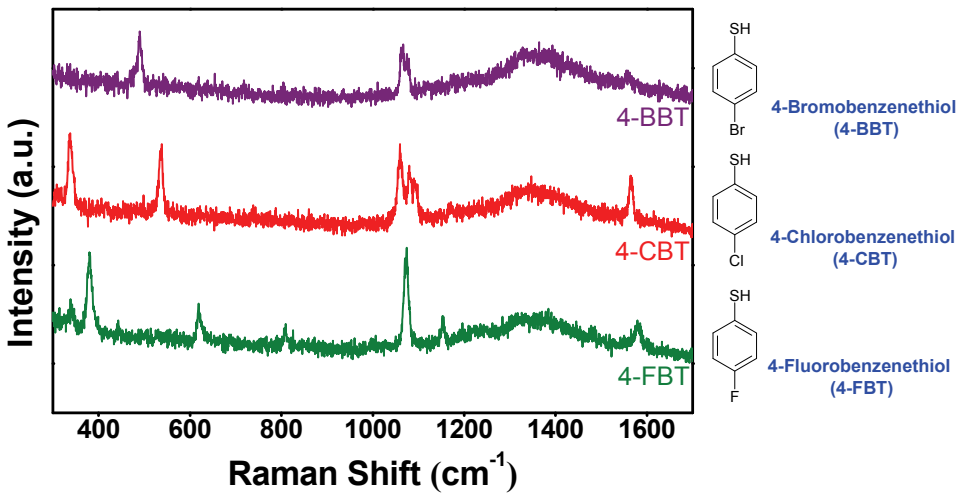

Figure 1-12. SERS spectra obtained from single Ag-Au SS probe particles coded with 4-BBT, 4-CBT, and 4-FBT.

Chemical structures of 4-BBT, 4-CBT, and 4-FBT are shown on the right side. All spectra were taken with 785-nm photoexcitation (390 μW at the sample) and 10 s acquisition time.

2. 5. Bio-application of Ag-Au SS probes

Finally, in order to demonstrate the potential applicability of Ag-Au SS as NIR SERS probe, a proof-of-concept experiment was performed in a mouse model. As shown in Figure 5a, a 10-μL aliquot of Ag-Au SS labelled with 4-FBT was subcutaneously injected at gluteal region of a nude mouse, and the SERS spectra were obtained using a Raman system with a 785-nm photoexcitation. The injected region exhibited the SERS signal which is well matched with the spectrum of 4-FBT-labeled Ag-Au SS probe, and no other distinctive Raman signal could be observed from normal skin region (Figure 5b). The intensity map of the 1075 cm^{-1} band exhibits that strong Raman signals of Ag-Au SS probes were easily detected in the probe injected region (Figure 5c). These results strongly suggest that the Ag-Au SS probes can be used for a sensitive detection of target biomolecules *in vivo*.

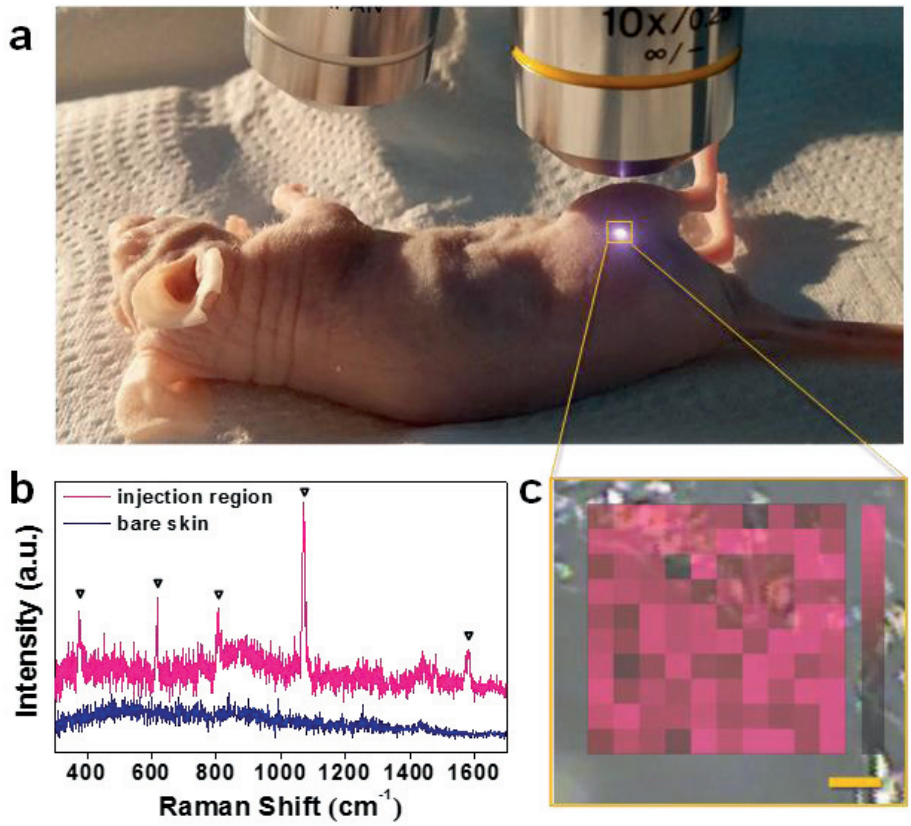

Figure 1-13. SERS detection using Ag-Au SS probes with NIR excitation.

(a) Photograph of Raman measurement setup for *in vivo* detection. (b) SERS spectra obtained from mouse skin with Ag-Au SS probes injected and without injected by the 785-nm photoexcitation of 43-mW laser power and 120-s acquisition time. (c) SERS intensity map of the 1075-cm^{-1} band of Ag-Au SS probes at the injected region. The mapping is 100 × 100 μm^2, which was scanned at 10-μm interval. The scale bar is 20 μm.

Chapter II. A Fast and Reliable Readout Method for Quantitative Analysis of SERS Nanoprobes on Chip Surface

1. Experimental

1. 1. Preparation of SERS dot dispersed substrate

Samples with different area densities of SERS dot particles were prepared by dropping small aliquots of the SERS dot solution on a slide glass. In order to evaluate quantitatively and correlate SERS intensity with the number of SERS dot particles on the chip surface, the optical images of the corresponding areas were analyzed with Image J program (National Institutes of Health, USA) to estimate the area density of SERS dot particles.

1. 2. Raman measurement

As an analysis tool for Raman measurement, a conventional micro-Raman system (LabRam 300, JY-Horiba, France) equipped with an optical microscope (BX41, Olympus, Japan) was utilized. In this system, the Raman scattering signals were collected in a back-scattering geometry and detected by a spectrometer equipped with a thermo-electrically cooled CCD detector. The 532-nm line of a diode-pumped solid-state laser (CL532-100-S, CrystaLaser, USA) was used as an excitation source. Focusing of the excitation laser lights and collection of Raman signals were accomplished

by the same 50× objective lens (NA 0.75, Olympus, Japan). The strong Rayleigh-scattering light was eliminated by a long-pass edge filter. During the measurement, sample power was set to be 1 mW using a neutral density filter.

Based on the analysis of readout methods, we designed a Raman readout system for quantification of chip-based bioassays. The 532-nm excitation light (Compass 115M, Coherent Inc., USA) was delivered via a galvanometric mirror of the laser scanning unit to a sample through a 40× objective lens (NA 0.75, Olympus, Tokyo, Japan). The back-scattered light from the sample was collected by the same objective and filtered by a holographic notch filter to remove Rayleigh scattering lights. Then, the light signal was focused onto the entrance slit of the spectrometer (XPE200, NanoBase, Korea) in order to be detected with a thermoelectrically-cooled CCD (charge-coupled device, Princeton Instruments). In order to perform whole area scan while minimizing scanning time, single spectrum per frame is obtained without saving individual spectrum by keeping CCD camera open during single raster scan of whole area with high confocal geometry.

2. Results and Discussion

2. 1. Preparation of Chip Samples

Three SERS-active nanoparticles were fabricated with three different Raman-labeled compounds (RLC: 4-FBT, 4-CBT, and 4-BBT). Each of them was named by SERS dot_{RLC} such as SERS $dot_{4\text{-FBT}}$, SERS $dot_{4\text{-CBT}}$, and SERS $dot_{4\text{-BBT}}$. As shown in Figure 1-1a, each SERS dot_{RLC} showed the unique SERS spectrum corresponding to each RLC, and representative bands were selected for multiplexed detection: The bands at 386, 541, and 492 cm^{-1} for 4-FBT, 4-CBT, and 4-BBT, respectively. Using SERS $dot_{4\text{-FBT}}$, four chip samples with different amounts of SERS particles on the surface were prepared. Samples (i) to (iv) in Figure 2-1a had an area density of 2.6%, 4.1%, 7.5%, and 21.6%, respectively, expressed in the percent ratio of particle area to the chip surface area.

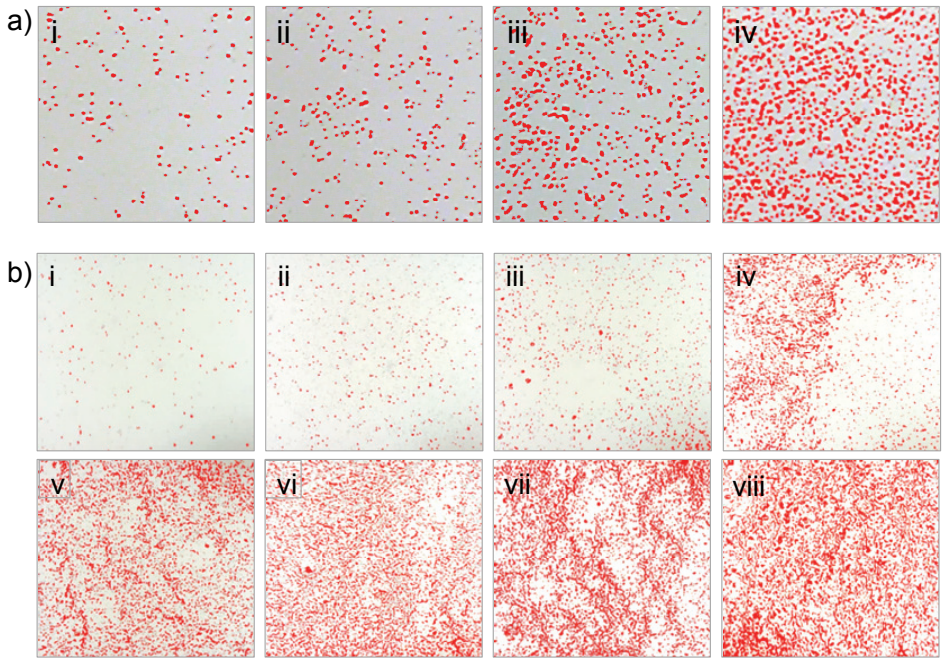

Figure 2-1. Images of prepared sample areas.

(a) Images of prepared sample areas (50 μm × 50 μm) with different area densities of SERS dots$_{4\text{-FBT}}$ of (i) 2.6%, (ii) 4.1%, (iii) 7.5%, and (iv) 21.6%. Each image is processed and analyzed for calculating the area density of SERS dot (area%) with Image J. SERS dots on the glass substrates were marked with red color on the images. (b) Optical images of samples (i)-(viii) with different area densities of SERS dots4-BBT. SERS dots were overlaid with red color via Image J. Each area is the 100 μm × 100 μm scale.

2. 2. Analysis of Raman readout modes

Assuming that we have a chip sample of 50 μm × 50 μm area and the beam diameter at a scanning spot in micro-Raman measurement is approximately 1 μm, we can choose either complete survey scan over the whole area demanding 50 × 50 points of measurement or sampled spot scan, whether random or periodic such as 5 × 5 points of measurement, while holding the same acquisition time per single spot of the same size. We analyzed the both modes of measurement in terms of sensitivity and reproducibility.

Four chip areas of 50 μm × 50 μm size from samples (i) to (iv) shown in Figure 2-1a were measured with two modes using micro-Raman point-mapping technique (50× objectives, beam diameter of ~1 μm, acquisition time of 1 s/point) as illustrated in Figure 2-2a. The complete survey mode reads the whole area by reading 50 × 50 points with 1-μm step size and is denoted as ‘mode A’. The other mode is a sampled spot scan that randomly reads partial area (25 points corresponding 25 μm^2) and is denoted as ‘mode B’. Each signal process in the different modes utilizing the different objcetives and acuisition times produced the different level of signal and noise signal, and resulted in mispresenting the spectra on a same axis scale. Therefore, Raman intensity was expressed as signal-to-noise ratio (SNR), by normalization of the scale with the standard deviation of the base line (the

noise level) in this study. Sensitivity of measurement was analyzed in terms of SNR defined as

$$SNR = (I_{signal} - I_{baseline})/I_{noise} \qquad \text{(eq. 2)}$$

where I_{signal} is the observed intensity of a Raman band, $I_{baseline}$ is the mean intensity where no Raman band appear, and I_{noise} is the standard deviation of the baseline.

For measurement with mode A, each SERS spectrum in Figure 2-2b (left) was obtained by one whole scan over 2,500 points and their summation since mode A covered the entire chip area of 50 μm × 50 μm. Meanwhile, for the measurement with mode B, each spectrum was obtained by summing 25 random spot scans (Figure 2-2b, right). The intensity at the 386 cm^{-1} band showed excellent linearity with the area density of SERS dots on chip for both measurement modes (Figure 2-2c). However, the sensitivity that is denoted as the slope of SERS intensity vs area density,[90-91] was 10 times less for mode B (slope = 15.2) than for mode A (slope = 146.4). In addition, we could analyze the reliability of the sampling survey (mode B) by plotting intensity of ten different sampling scans of each sample with area densities of SERS dots. From the 25 spectra that were randomly obtained for each scan, SERS intensities at the 386 cm^{-1} band were plotted as open circles with the averaged value for 10 scans as red squares in Figure 2-3. Despite

good linearity of the averaged SERS intensitiy as shown in Figure 2-2c, the sample survey with the measurement mode B led to large fluctuation in signal intensity. Table 2-1 illustrates that the relative standard deviation (RSD, %) was considerably large and became even larger with a decrease of the area density of SERS dots. This finding indicates that signal intensity became less reproducible for lower concentrations of analytes even though the signal was detectable. This result forced us to find alternate measurement method that is practical in terms of measurement time and holds reliability of the complete survey method.

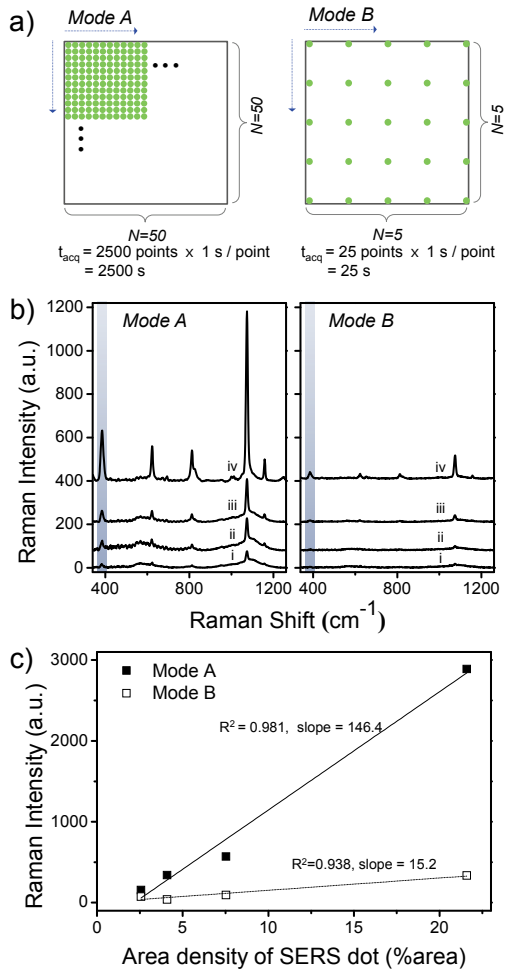

Figure 2-2. Comparative analysis of the complete survey and sampled spot scanning methods for quantitative Raman readout.

(a) Schematic illustration of different readout modes. Mode A is a complete survey scan mode and mode B is a sampled spot scanning mode. (b) The average SERS spectra from the samples (i)-(iv) (from bottom to top, respectively). The spectra on the left panel were obtained by mode A, and the spectra on the right panel by mode B. (c) Intensity plot of 386 cm^{-1} band with increasing area density of SERS dot$_{4\text{-FBT}}$ for modes A and B.

Table 2-1. SERS intensities of sample (i) - (iv) from mode B. Mean values, standard deviations (SD), and relative standard deviations (RSD, %) were obtained from 10 repeat scans in Figure 2-2.

Sample	i	ii	iii	iv
Area density of SERS dot (%area)	2.6	4.1	7.5	21.6
Mean of signal intensity	35.6	58.0	221.7	530.8
SD	24.0	27.2	89.2	140.1
RSD[a] (%)	±67.4	±46.8	±40.2	±26.4

[a] Relative standard deviation (RSD); RSD = 100 × (Standard deviation)/(Mean)

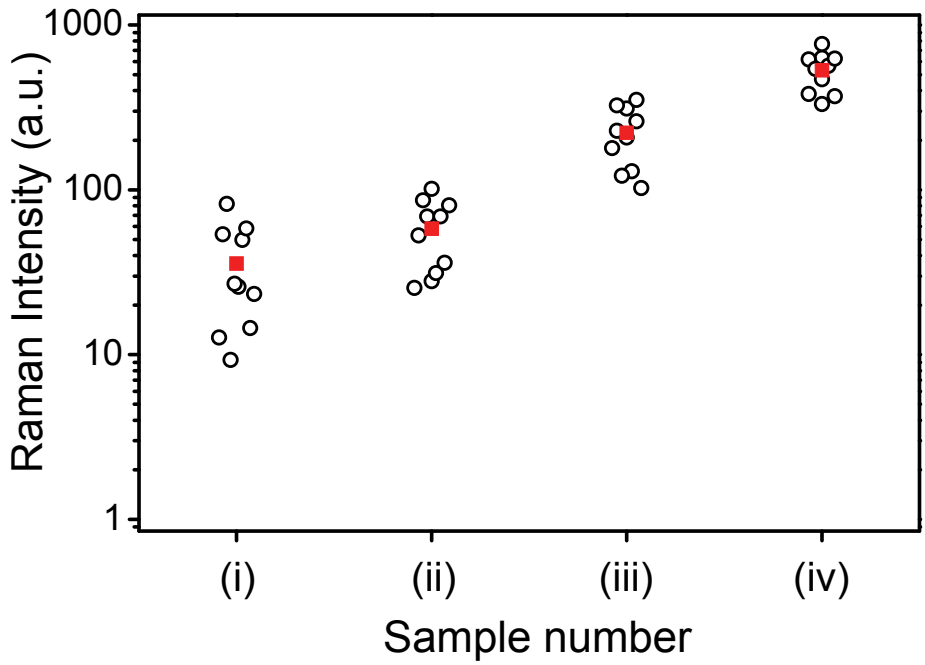

Figure 2-3. Signal fluctuations among randomly extracted 25 spectra (mode B) from sample (i) - (iv).

The distributions of signal intensity (386 cm^{-1}) from each averaged spectrum are denoted as black circles (○) from 10 repeat scans. The mean values of each sample are expressed as red squares (■).

2. 3. Analysis of scanning methods for whole area measurement

The complete survey measurement with mode A in the previous section consumed a massive amount of time since total acquisition time is acquisition time of single spot (i.e. 1 s, here) multiplied by number of spots (i.e. 2,500). Furthermore, the motorized XY stage in a microscope and the CCD detector require additional time for physical operations. There are two approaches for reducing the total measurement time while maintaining the whole area-scanning strategy. One approach (mode C) involves reducing the acquisition time per spot while maintaining the same illuminated beam size as mode A. The other approach (mode D) involves enlarging the beam size and FOV for signal collection while maintaining the acquisition times per spot the same as mode A.

Figure 2-4a illustrates three modes of whole area-scanning. Mode A is the same as in Figure 2-2a; mode C performs 50 × 50 scans with ~1-μm beam size and decreased acquisition time (0.01 s/spot), thereby resulting in the total acquisition time of 25 s. Mode D does 5 × 5 scans with approximately 10 times an enlarged beam size and collection area (~10 μm^2 using 5× objective) and the same acquisition time (1 s/spot) as mode A, thus resulting in the total acquisition time of 25 s. The sample (iv) was chosen in this

measurement, and the summed spectra for each mode are shown in Fig. 3b. As expected from 100 times reduced total acquisition time, modes C and D revealed much lower signal intensity than mode A. However, it is important to note that mode C had much larger signal intensity and less background features of glass substrate than mode D. The increased noise signal in mode D can be attributed to increased light collection from depth down the substrate by using a lower magnitude objective. Therefore, in terms of sensitivity in the assay, keeping higher confocality in signal collection appeared to be more favorable than enlarging FOV under the same total acquisition time.

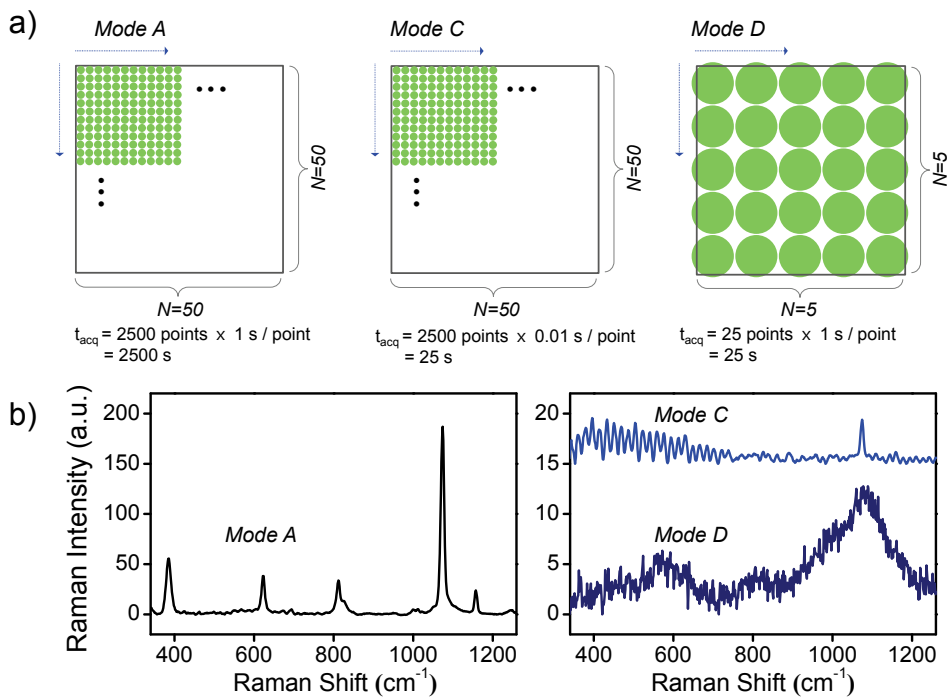

Figure 2-4. Analysis of scanning modes for whole area measurements on the 2-dimensional surfaces.

(a) Schematic illustration of different scanning modes. (b) The averaged spectra from the sample (iv) obtained by mode A, C and D.

2. 4. Design and validation of a fast and reliable Raman readout system

Regarding a conventional microscope-based Raman instrument, point-scanning or line-scanning were generally utilized for quantitative measurements over a 2-dimensional surface area. Readouts of whole areas could achieve the increased reliability for the quantitative measurement, but it costs too long measurement time. Considering the factors that can reduce total acquisition time and allows for reliable data by scanning whole area, we demonstrated a fast Raman scanning method for quantitative readout of chip-based immunoassays (Figure 2-5). This method adopted a 2-dimensional raster scanning of whole area and signal collecting algorithm that accumulates collected signals in CCD during one whole-area scan and then gives a single spectrum per frame. This method saves time for data processing from CCD to PC and for controlling 2-D scanning while allowing a whole area scan. The 2-D scanning unit involves mirror control that is turned galvanometrically and moved by an actuator simultaneously. The turning axis and the moving axis of the mirror were arranged perpendicular to each other, thereby resulting in a single mirror that can deflect the laser beam moving fast in the direction of the X-axis and shifting slowly in the direction of the Y-axis simultaneously. After the beam was deflected by the mirror, the beam was focused on the sample through a focusing lens. Maximum scanning area was a scale of 200 μm × 200 μm, which is limited by confocality with 40× objectives.

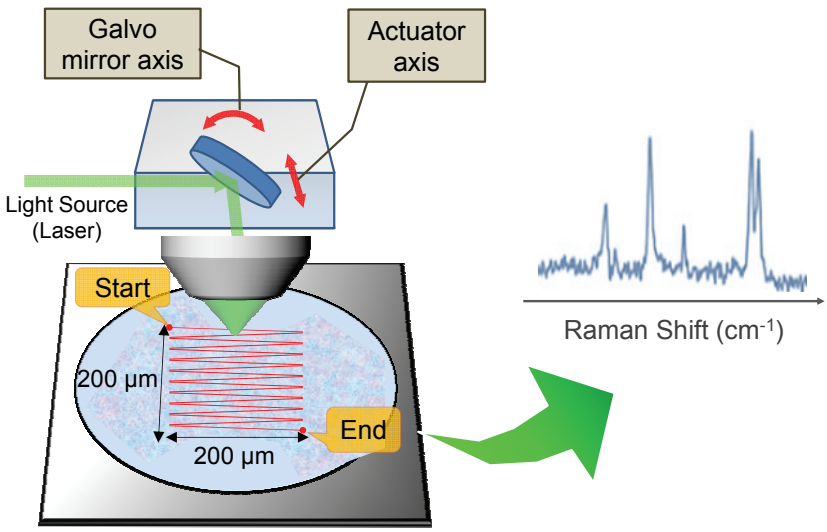

Figure 2-5. Schematic illustration of quantitative Raman measurement by fast Raman scanning method with confocal scanning.

Total area-scanning was performed for 2-dimensional readout by galvo-mirror and actuator.

Validation of this approach was performed by comparison of the two readout modes as shown in Fig. 5a. The first mode is whole area scan (left), and the other one is sampled spot scan (right). The 40× objective lens (NA 0.75, ~1 μm in diameter) was utilized, and the sample power was 2 mW. In the whole area-scanning mode, a confocal laser beam was exposed tightly to the sample area by a raster-scanning with 40 Hz frequency. This mode of measurement resulted in summed SERS spectrum of which signals were obtained as fast as 10 s for one scan over the whole area. In the sampled spot scanning mode, the laser beam was exposed to 25 points of the sample area, and the total acquisition time was 10 s (0.4 s/spot). The 100 μm × 100 μm areas of two samples with 7.1% (sample I) and 2.9% (sample II) of SERS dot$_{4\text{-FBT}}$ on the substrate surfaces were analyzed. Fig. 5c shows the spectra for two different measurements. The whole area-scanning mode exhibited a 1.7-fold signal of the 386 cm^{-1} band than the sampled spot scanning mode. In the case of sample II that has a lower area density of SERS dots, the sampled spot scanning mode detected little signal of SERS dots (SNR of 0.2 at 386 cm^{-1}) whereas the whole area-scanning mode exhibited significant SNR of 5. This result indicates that superior sensitivity can be obtained by the whole area scanning mode and was more prominent in the sample of the lower area density of particles as well as the inherent

fluctuation of signals from the sampled spot scan shown in Figure 2-3. Consequently, we confirmed that the proposed method of whole area-scanning has advantages in terms of efficient experimental time, higher sensitivity, and greater reproducibility for applications of chip-based immunoassay.

Next, sensitivity and reliability of this readout method over different area density were characterized by analyzing the signals of SERS dots$_{4\text{-BBT}}$ in comparison with the results in Figure 2-2. For this analysis, eight samples with different area densities of SERS dots$_{4\text{-BBT}}$ were prepared as shown in Figure 2-1b. Each SERS spectrum was obtained by whole area-scanning over 100 μm × 100 μm area with total acquisition time of 10 s (Figure 2-6a). The least square linear fit of the signal of the 492 cm^{-1} band of 4-BBT and the area density (%) exhibited high linearity of $R^2 = 0.996$, which is as good as in the complete survey with mode A and much higher than the value in the sample survey with mode B (Figure 2-2 and Table 2-1). The slope as a measure of sensitivity was 3.8 times higher than mode B and 2.5 times lower than mode A whereas the total scanning time was only 10 s. This result illustrates that this method is a quite good compromise for measuring time efficiency with slight sacrifice of sensitivity for quantitative analysis of SERS nanoprobes on chip surfaces. The limit of detection of this system

under the current condition was estimated to be 300 particles in a 100 μm × 100 μm area.

The feasibility of multiplexed quantification was tested for this method. The surface areas on which two SERS dots (SERS $dot_{4\text{-FBT}}$ and SERS $dot_{4\text{-CBT}}$) were co-dispersed with 1:1 ratio were examined (Figure 2-8). The 386 cm^{-1} band of 4-FBT and the 541 cm^{-1} band of 4-CBT were chosen, and their normalized intensities, which are defined as the observed Raman intensity of a sample divided by that of the sample with the highest area density of SERS dots, were used for analysis since two Raman bands have different peak intensities each other. The plot of the normalized Raman intensity of both SERS dots exhibited good linearity with the particle density of the SERS dots as shown in Figure 2-8b. In this respect, this approach was considered to perform successfully for quantitative multiplexing Raman analysis on chip surfaces.

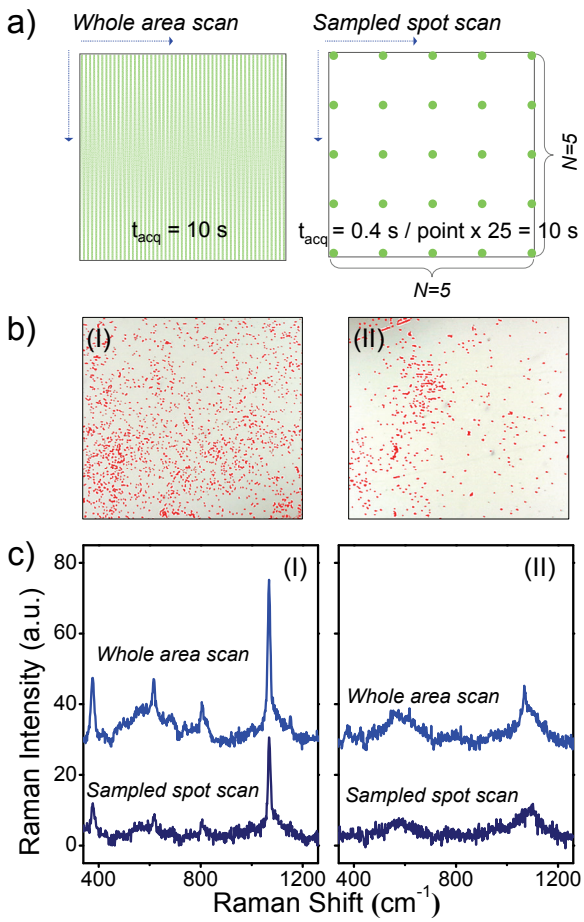

Figure 2-6. Comparison of Raman intensity with different measurement modes for quantitative Raman readouts on the 2-dimensional surfaces.

(a) Schematic illustration of whole area scanning mode and sampled spot scanning modes. Total acquisition time is 10 s in each measurement. (b) Images of measured sample areas (100 μm × 100 μm) with area density of SERS dot$_{4\text{-FBT}}$ of 7.1% (sample I) and 2.9% (sample II). SERS dots on the glass substrates were marked with red color on the images. (c) The spectra from the sample area obtained from each method. The spectra are expressed in the unit of Raman signal intensity with normalization by noise level.

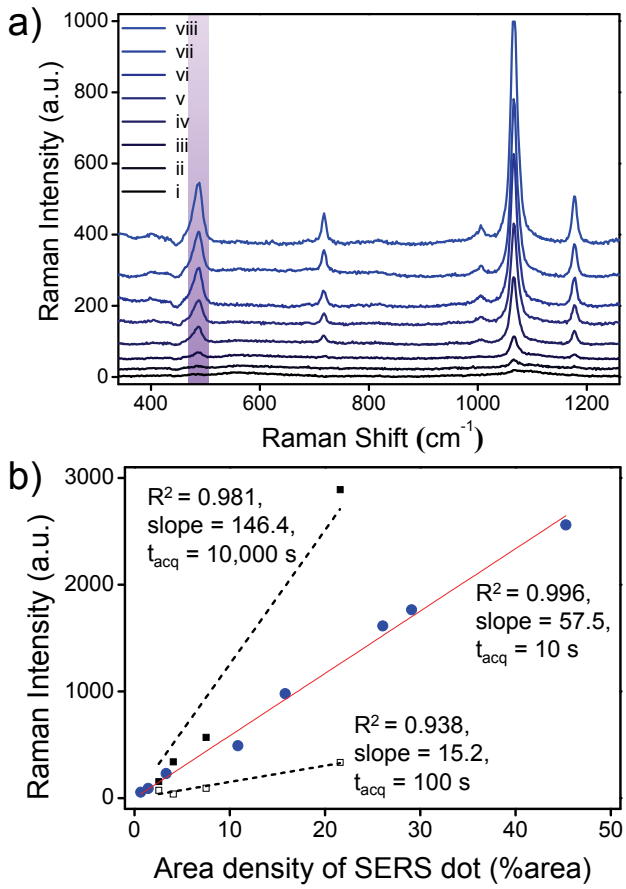

Figure 2-7. Demonstration for the correlation between the particle densities of SERS dot$_{4\text{-BBT}}$ on the glass surface and the corresponding SERS intensities.

(a) Raman spectra from 100 μm × 100 μm areas of different area densities of SERS dot (% area): (i) 0.6%, (ii) 1.5%, (iii) 3.3%, (iv) 10.9%, (v) 15.8%, (vi) 26.0%, (vii) 29.1%, and (viii) 45.2%. (b) Correlation plot (red) between the particle densities of SERS dot$_{4\text{-BBT}}$ and the Raman intensities at 492 cm^{-1} band of 4-BBT from (a). Dashed lines are preceding data that are exhibited in Fig. 1c. Acquisition time (t_{acq}) was recalculated at a standard for 100 μm × 100 μm area.

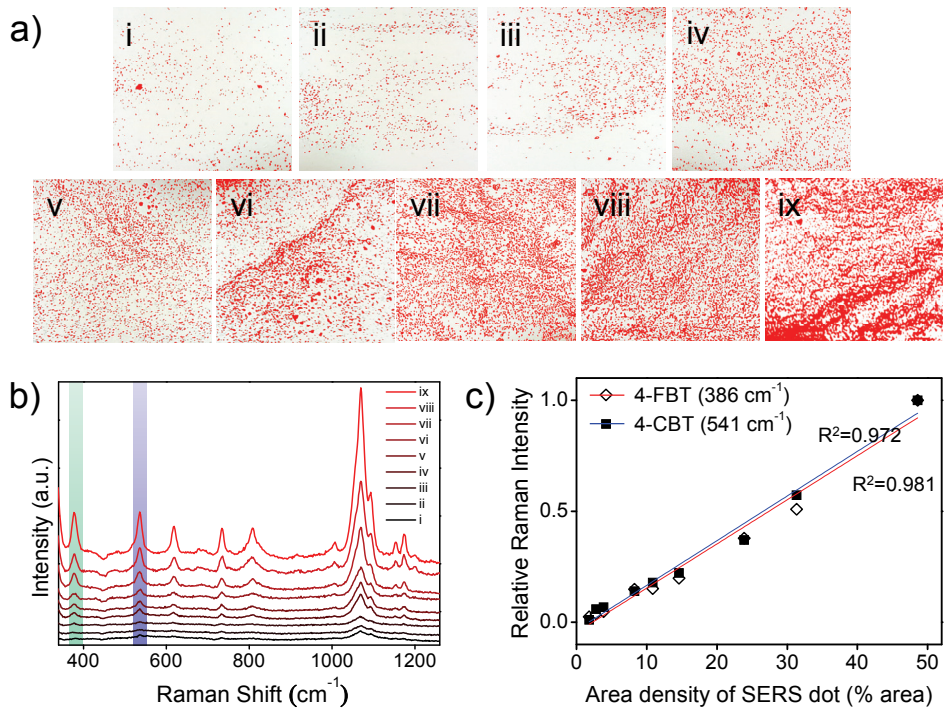

Figure 2-8. Demonstration of multiplexed quantification via the whole area scanning method.

(a) Optical images of samples on which SERS dots$_{4\text{-FBT}}$ and SERS dots$_{4\text{-CBT}}$ were co-dispersed with 1:1 ratio. SERS dots were overlaid with red color. Each area is 100 μm × 100 μm scale. (b) Raman spectra from samples (i)-(ix) of (a). Each spectrum was obtained by Fast Raman Scanning with acquisition time of 10 s, and the sample power of the excitation laser was 2 mW. (c) Correlation plots between the area densities of SERS dots and the relative Raman intensities at 386 cm^{-1} band of 4-FBT and 541 cm^{-1} band of 4-CBT from (a) and (b).

*Relative Raman intensity = (the observed Raman intensity of a sample)/ (the observed Raman intensity of the sample with the highest area density of SERS dots).

Chapter III. On-chip SERS-based Immunoassay with Femtomolar Sensitivity and a Broad Dynamic Range Using SERS Nanoprobes and an Area-Scanning Method

1. Experimental

1. 1. Chemicals and Materials

N-hydroxysuccinimide (NHS), *N*,*N*-diisopropylcarbodiimide (DIC), *N*,*N*-diisopropylethylamine (DIPEA), 4-dimethylaminopyridine (DMAP), phosphate-buffered saline (PBS; tablet) and bovine serum albumin (BSA, > 98%) were purchased from Sigma-Aldrich (St. Louis, MO, USA). Epoxide-functionalized slide glasses were purchased from Arrayit Corporation (Sunnyvale, CA, USA). Two types of anti-PSA antibody (PSA10 & PSA66) were purchased from FUJIREBIO (Tokyo, Japan). Cy5® Goat Anti-Mouse IgG and Alexa Fluor® 555 microscale protein labeling kit were purchased from Molecular Probes (USA).

1. 2. Bio-functionalization of SERS dot

In order to bio-functionalize the SERS dots, the following steps of surface modification were proceeded. First, 1-mg of SERS dots was dispersed in 1-mL of 5 *v*/*v*% APTES solution in ethanol, and 10 μL of NH_4OH (27%) was added. The resulting mixture was shaken for 1 h at 50 °C and washed with ethanol several times, and then re-dispersed in 500 μL of NMP. Succinic anhydride (1.75 mg) was added to the APTES-treated SERS dot dispersion,

followed by addition of 3.05 μL of DIPEA to introduce carboxyl group on the SERS dot. The resulting mixture was stirred for 2 h at room temperature. Subsequently, the carboxyl group-functionalized SERS dots were washed with NMP and then redispersed in 200-μL of anhydrous NMP. For activation of the carboxyl group, NHS (20 mg), DIC (27 μL), and DMAP (2.1 mg) were added to the dispersion. The resulting dispersion was stirred at room temperature for 1 h and then washed with NMP and PBS (pH 7.4). A 25-μg of tracer antibody was added to the NHS-activated SERS dots dispersed in 200-μL of PBS. The mixture was incubated for 1 h at room temperature. The resulting dispersion was washed with PBS containing 0.1*w/w*% Tween 20 (TPBS), and redispersed in PBS after BSA (5*w/w*% in PBS) treatment. After removing the excess reagents by centrifugation and washing, tracer antibody-conjugated SERS dots were dispersed in PBS and stored at 4 °C before use.

For evaluation purpose of bio-functionality of SERS dots, fluorescence labeled PSA was used as follows. Five micro-liter of 1 mg/mL antibody-conjugated SERS dot solution (3×10^{11} particles/mL) was mixed with 45 μL of Alexafluor555-labeled-PSA solutions of various concentrations (0.01 – 200,000 ng/mL). Under mild shaking, the resulting dispersions were incubated for 3 h, and sequentially washed with TPBS several times. Finally, the SERS

dots were re-dispersed in PBS (15 μL) before measurement. PSA-bound SERS dots dispersion was filled in a capillary tube and fluorescence signals were measured with a micro-Raman system (JY-Horiba, LabRam 300).

1. 3. Preparation of capture substrate and immunoassay protocol

For fabrication of a capture substrate, the 96 spots arrayed sticker (Proteogen, Chuncheon, Korea) was attached on an epoxy-functionalized glass slide. The 1.5-μL aliquots of 100 μg/mL tracer antibody solutions were incubated on the arrayed spots of the substrate for 4 h in a humidity chamber at room temperature. Then, the slide was soaked in TPBS and PBS with shaking to remove unbound antibodies from the substrates for 7 minutes. The remaining non-reacted epoxy groups were blocked with ethanolamine (10 mM) in PBS for 30 min, and the unreacted reagents were washed with TPBS and PBS. The substrates were stored in PBS at 4 °C before use.

In assay procedures, the capture substrate was exposed to the 1.5-μL aliquots of analytes (PSA) serially diluted with PBS containing 1*w/w*% BSA for 1 h in a humidity chamber. The three trials were replicates of each concentrations of 0.001 − 1000 ng/mL. After washing with TPBS

and PBS, the antigen-captured substrate was exposed to 1.5 μL of the tracer antibody-conjugated SERS dots dispersion for 2 h. Finally, the substrates, on which sandwich immunocomplexes were formed, were rinsed with TPBS, PBS and D.I. water, followed by drying gently with a stream of nitrogen gas.

1. 4. Immunoradiometric assay (IRMA) and chemiluminescence immunoassay (CLIA) for PSA analysis

PSA levels were measured by using the IRMA commercial kit (Ultra PSA IRMA tube; Shin Jin Medics, Korea), having a functional sensitivity of 0.01 ng/mL. Briefly, all kit components and samples were stored at room temperature. All liquid reagents including samples were agitated gently before use. Standard solution, controls, PSA samples (50 μL) were pipetted into test tubes coated with anti-h-PSA (polyclonal, rabbit). The tubes were briefly agitated on a sample mixer and incubated for 30 minutes at the room temperature. Next, 2 mL of the washing solution was added and the tube was washed twice. The tubes were placed upside down on an adsorbent paper for a minimum of 10 minutes. Finally, 50 μL tracer of ^{125}I-labeled monoclonal anti-PSA antibody was pipetted into each tube. The tubes were incubated for

30 min at room temperature with shaking (200–300 rpm) and washed twice again with 2 mL of the washing solution. All tubes were placed upside down on an adsorbent paper for at least 10 min twice. Radioactivity of each tube was measured by using a gamma counter (Gamma-10; Shinjin medics, Goyang, Korea) with countable isotope energy of 15–2000 keV.

PSA levels of the same samples were measured also by using chemiluminescence immunoassay (CLIA) method. For the measurement, Cobas instrument and Elecsys (Roch Diagnostics, USA) were used. Its functional sensitivity is 0.03 ng/mL. Twenty micro-liter of sample was incubated with a biotinylated monoclonal PSA-specific anti-body and a monoclonal PSA-specific antibody labeled with a ruthenium complex. After the addition of streptavidin-coated microparticles, the complex becomes bound to the solid phase via interaction of biotin and streptavidin. The reaction mixture is aspirated into the measuring cell where the micro-particles are magnetically captured onto the surface of the electrode. Unbound substances are then removed with ProCell. Application of a voltage to the electrode then induces chemiluminescent emission which is measured by a photomultiplier. Results are determined via a calibration curve which is instrument-specifically generated by 2-point calibration and a master curve provided via the reagent bar code.

1. 5. Instrumentations

The spot-arrayed slide was scanned with GenePix 4000B (Axon Instruments, CA, USA) scanner using 532-nm or 635-nm laser-line for characterization of antibody immobilization and antigen-antibody interaction using Cy5-labled antibodies and Alexafluor555-labeled antigens. The scanner was set to optimize the quality of the microarray images by adjusting the laser power and contrast. The signal intensity was quantified with GenePix Pro 3.0 software (Axon Instruments, CA, USA).

For obtaining fluorescence spectrum, a conventional confocal microscope Raman system (LabRam 300, JY-Horiba, France) equipped with an optical microscope (BX41, Olympus, Japan) was utilized with changes of 10× objective lens and 300 grooves/mm grating.

2. Results and Discussion

2. 1. Design of SERS–based Immunoassay

To develop a reliable and sensitive immunoassay with a wide dynamic range, two approaches were combined in our SERS based immunoassay platform (Figure 1): 1) assembled-metal SERS nanoprobes, termed SERS dots,[32,79] and 2) a full-area confocal raster scanning method for rapid and reliable chip analysis.[78] Antigens and SERS dots were applied to the capture antibody-conjugated glass slide to generate immunocomplexes. Subsequently, SERS signals from a large area of the glass slide (10,000 μm^2) were measured with the full-area confocal raster scanning method.

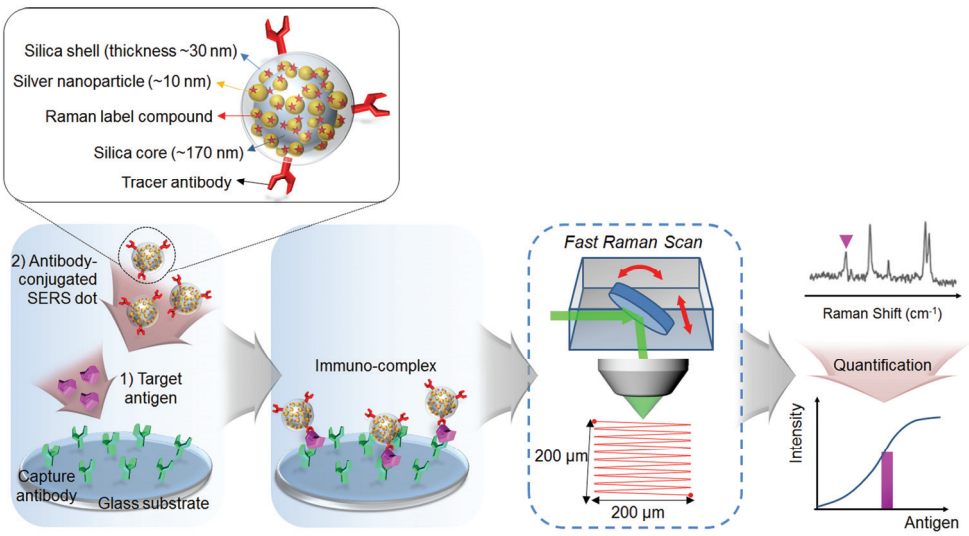

Figure 3-1. Schematic illustration of a chip-based immunoassay using SERS dots and an area-scanning readout system.

SERS dots were fabricated by in situ synthesis and introduction of Ag NPs on the silica core, followed by Raman labeling and silica encapsulation. SERS dots were conjugated to tracer antibodies. The capture antibody-immobilized glass substrate was incubated with target antigen and tracer antibody-conjugated SERS dots sequentially. After selective tagging of captured antigens with SERS dots, readout by Raman spectroscopy and analysis of the dose-response relationship using a calibration curve were performed.

2. 2. Evaluation of bio-functionality of SERS dots

For bio-functionalization of SERS dots, further surface modifications after fabrication of SERS dots were performed after fabrication of SERS dots (Figure 3-2a). For conjugation with tracer antibody via amide bonding, SERS dots were carboxyl-functionalized by two step reactions. Subsequently, the carboxyl groups were activated for amide bond formation with amine groups of tracer antibody. We explored the activation protocols using silica NPs, and the results from fluorescence signal of Cy5-labeled antibody showed that the reaction conditions with excess NHS achieved antibody immobilization successfully (Figure 3-2b). As the activated NHS groups are unstable in aqueous condition, excess NHS was required. We observed that the different antibody concentrations also lead to different densities of antibody immobilized on surfaces of silica NPs (Figure 3-3a). We could estimated the number of antibody immobilized on a single NP using the measured antibody concentrations of the colloidal solutions via standard curve (Figure 3-3b) of pure Cy5-IgG solutions and initially known concentraions of Si NPs. In our experimental conditions, the density reached plateau over 0.6 mg/mL of Cy5-IgG concentraions, and the maximum number of immobilized antibody was nearly ~55 on a single silica NP. The varied conditions could immobilize more antibodies on the surface, because the surface was not fully saturated considering the size of particles.

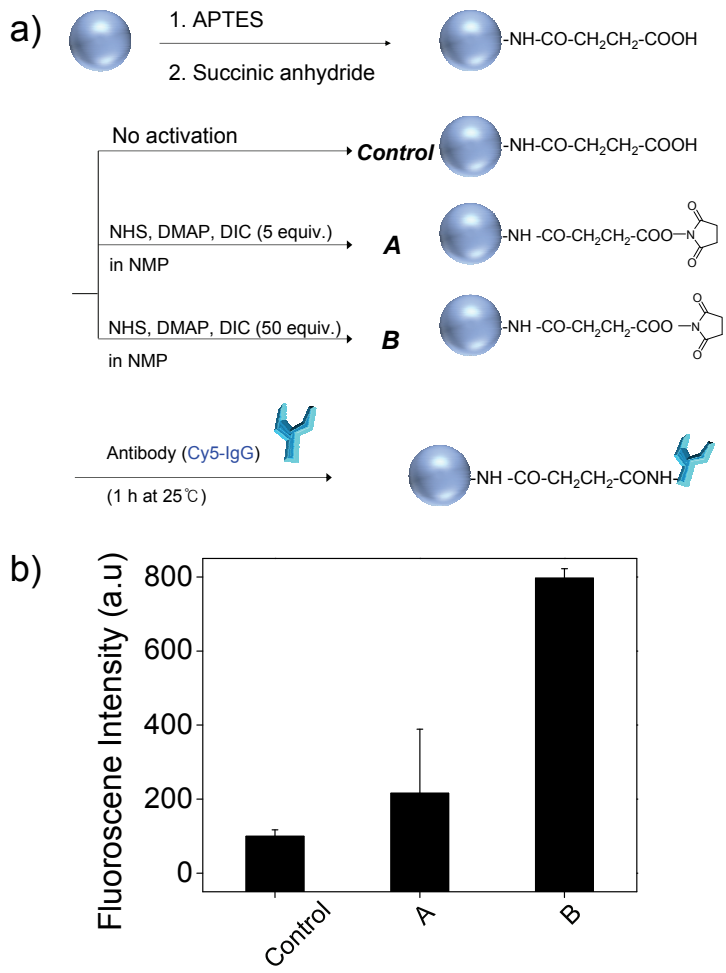

Figure 3-2. Antibody immobilization on Si NPs via covalent bond formation with different carboxyl-activation conditions.

(a) Experimental scheme of surface modification for biofunctionalization of silica nanoparticles. The experiments were designed to achieve immobilization of antibody on the silica surface via amide bonding formation. Functionality was examined as 3.5 μmol per 1 mg of SERS dots. (b) Comparison of fluorescence intensity.

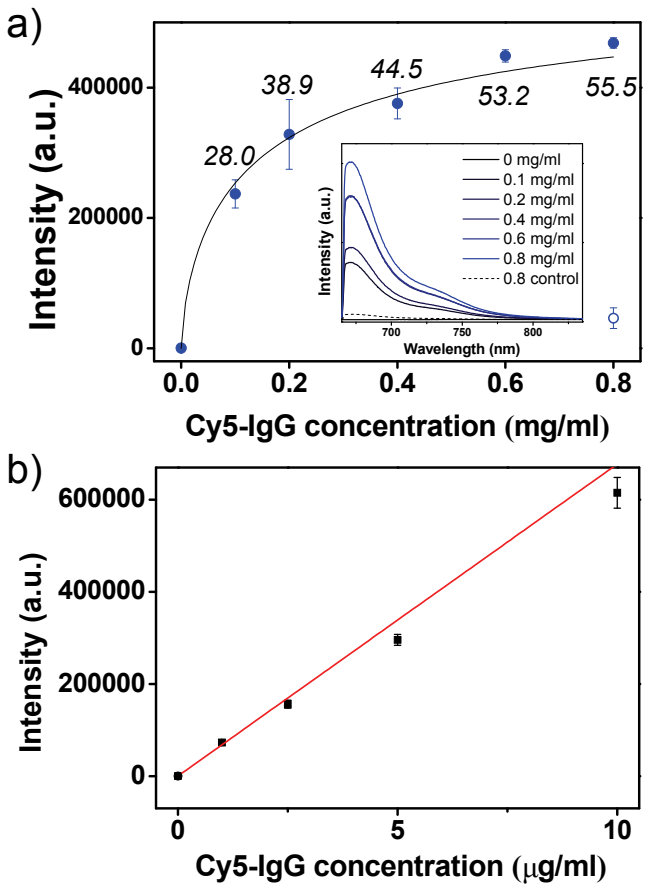

Figure 3-3. Antibody immobilization on the nanoparticles with different antibody concentration conditions.

(a) Fluorescent intensities as incubated fluorescent labeled antibody (Cy5-IgG) concentrations increased. (b) Standard curve obtained from fluorescence intensities of different concentrations of Cy5-IgG solutions. The numbers on the each point of (a) means the number of immobilized antibody on a single silica NPs, while the estimation was obatained from (b).

In respect of specific binding, we examined the bio-functionality of the SERS dots after antibody conjugation and stabilization. Antigen-capturing activity of the SERS dots was demonstrated using Alexafluor555-labeled PSA (AF555-PSA). As illustrated in Figure 3-4a, the anti-PSA antibody-conjugated SERS dot (anti-PSA-SERS dot) solutions (1.5×10^9 particle) were incubated with various concentrations of AF555-PSA solutions (0.01 – 200,000 ng/mL) and washed out to remove unbound antigens. The anti-epidermal growth factor receptor (EGFR) antibody conjugated-SERS dots were used for a negative control experiment in the same way. From the fluorescence spectra (Figure 3-3b,c), signal intensities were plotted as function of AF555-PSA concentrations as shown in Figure 3-3d. The fluorescence intensities of AF555-PSA treated anti-PSA-SERS dots solutions increased with increase of AF555-PSA concentrations, while the anti-EGFR antibody-conjugated SERS dot solutions showed negligible increase of the signal intensities.

To evaluate the antigen binding capacity of PSA-SERS dots, the number of bound AF555-PSAs was estimated using the standard curve obtained from fluorescence signal intensities of free AF555-PSA (Figure 3-3e). For the case of SERS dots with the highest fluorescence intensity, the antibody concentration was estimated to 97.9 ng/ml from the standard curve. That

means that the final solution (15 μL) contained 2.7×10^{10} PSA molecules bound to SERS dots, and the number of PSA molecules captured on a single antibody-conjugated SERS dot was 18 in average.

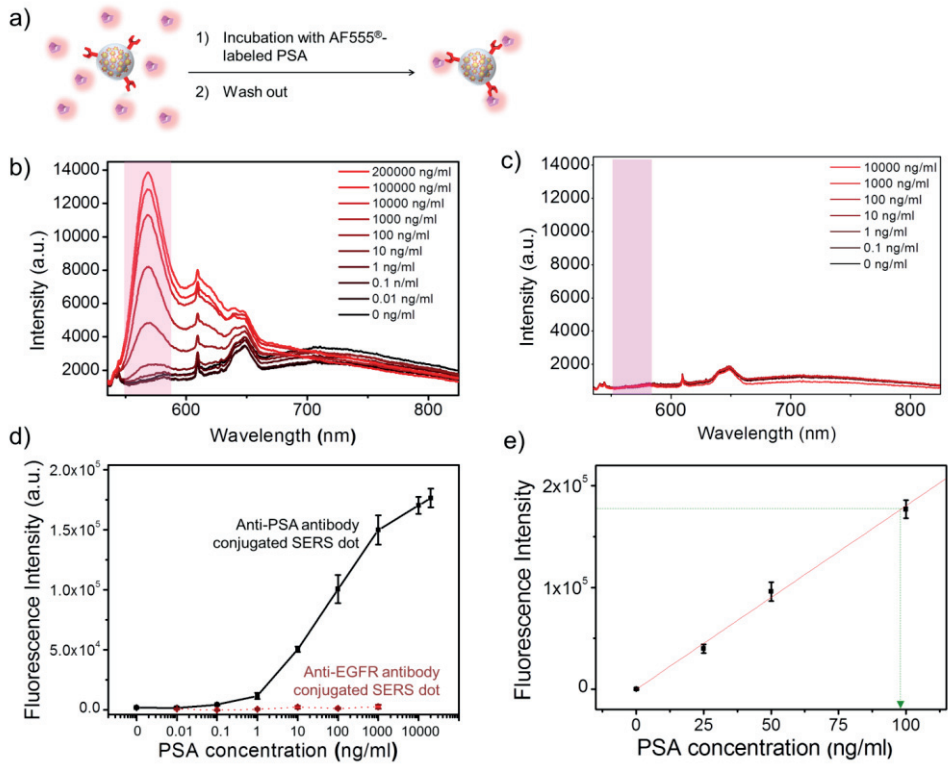

Figure 3-4. Bio-functionality test of tracer antibody conjugated-SERS dots via binding of target antigen (PSA).

(a) Schematic illustration of bio-functionality test of tracer antibody conjugated SERS dot. (b) Fluorescence spectra of anti-PSA antibody conjugated SERS dot after binding with different concentration of alexafluor®555-labeled PSA. (c) Fluorescence spectra of anti-EGFR antibody conjugated SERS dot after binding with different concentration of alexafluor®555-labeled PSA. (d) Analysis of fluorescence intensity with increasing PSA concentrations from (b) and (c). (e) Standard curve obtained from fluorescence intensity of free alexafluor®555-labeled PSA solution.

When considering that we had controlled the condition to immobilize the antibodies of ~28 on a single surface (Figure 3-3a), we could estimate the 18/28, *i.e.*, ~64% of antibody capturing the antigens.

The colloidal stability of antibody conjugated SERS dot particles was also demonstrated with respect to multiplexing capability of the nanoprobes. When the different fluorescence-labled antibodies are mixed, the aggregation of antibodies could be issue due to the conformational changes.[92] In order to utilize the antibody conjugated nanoprobes in a multiplexed immunoassay, the collodial stability is required to be garanteed. When the two different antibodies (anti-PSA ab, M.W. 150 kDa; anti-7proPSA , M.W. 55 kDa) immobilized SERS dots were mixed, we observed that the sizes of the nanoprobes were unchanged, implying the aggregation did not occur (Figure 3-5). This result reveals the stability of nanoprobes, therefore the antibody conjugated SERS dot could be evaluated to be suitable for multiplexed in terms of colloidal stability.

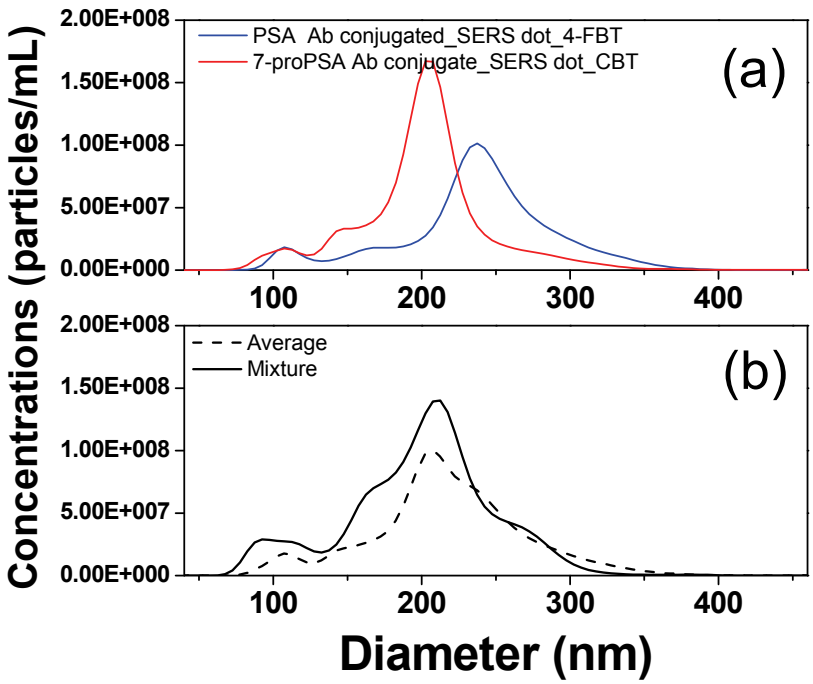

Figure 3-5. Colloidal stability of antibody conjugated SERS dots.

Size distributions of (a) anti-PSA antibody conjugated SERS dots and anti-[-7]proPSA antibody conjugated SERS dots, and (b) their mixture (solid line). Compared to arithematical average of the two (dashed line), the size distribution of mixture are not quite differnt, exhibiting no aggregated features.

2. 3. Development of Assay protocols

For developing of sensitive immunoassay, optimizations of various experimental conditions were required. First, optimization of antibody immobilization step was needed for fabricating capture substrate, because antibody surface density is important in terms of detection sensitivity.[93-94] Increased surface density of capture antibody generally offers improved capturing capacity of target antigen.[95] To determine the antibody-saturated condition, fluorescence based analysis was carried out using Cy5-Ab. An epoxy-functionalized slide glass was incubated with the various concentrations of Cy5-Ab solutions (0.01, 0.1, 1, 10, and 100 μg/mL) for different times (0.5, 1, 2, 4, and 8 h) to allow the reaction between the epoxy groups and the free amine groups on the surface of the antibody. As a result, fluorescence scanning images (Figure 3-6a) show that the higher concentration and the longer incubation time led to higher density of capture antibody immobilization. As shown in Figure 3-6b, in case of antibody concentrations below 1 μg/mL, degrees of antibody immobilization were linearly increased with incubation times. In case of 10 μg/mL of antibody concentration, the chip surface was gradually saturated for 4 h. When 100 μg/mL of antibody solution was applied, the chip surfaces become nearly saturated within 1 h, and immobilization of antibody was completely

accomplished in 2 h. Through these results, we found optimized immobilization condition, such as the 4 h for incubation time and the 100 μg/mL for antibody concentration, to guarantee high density of capture antibody.

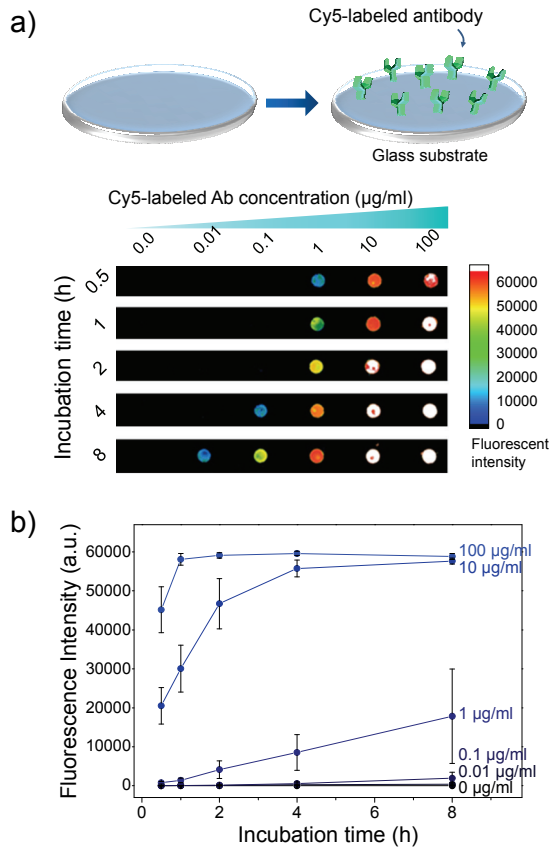

Figure 3-6. Antibody immobilization on the substrate with different incubation conditions.

Degree of immobilization of antibody was determined by fluorescence intensity of cy5-labeled anti-mouse IgG. (a) Fluorescence scanning image of spot-arrayed slide with different incubation time (0.5 h, 1 h, 2 h, 4 h, and 8 h; from the top down) and antibody concentration (0.01 - 100 μg/mL). (b) Analysis of fluorescence intensity with increasing incubation time. After 2 h, immobilization of antibody was saturated at 100 μg/mL of the antibody concentration. Error bars indicate standard deviations from six repeats.

The experimental conditions during on-chip antigen-capture also needed to be optimized for removing nonspecific binding related to sensitivity of the immunoassay. AF555-PSAs with concentrations of 0.01 − 10000 ng/mL were used to confirm the on-chip antigen binding. Before incubation with AF555-PSA solutions, 10 mM of ethanolamine solution (in PBS, pH7.4) was used for capping of residual epoxide groups on glass surface. And, AF555-PSAs were incubated with BSA (1*w/w* %) or without BSA to explore the blocking effect of BSA.

The fluorescence scanning images (Figure 3-7a) of AF555-PSAs show that the existence of BSA in PSA solution could successfully prevent the nonspecific binding. On the negative control spot (no capture antibody, and 1 ng/mL of PSA was applied), nonspecific binding was significantly reduced under existence of BSA (Figure 3-7b). Interestingly, as shown in Figure 3-6c, the slope and linearity of dose-response curve (plots of fluorescence intensity vs AF555-PSA concentrations in log scale) was higher in case of existence of BSA (slope=0.9493, $R^2 = 0.93$) compared to that of without BSA (slope=0.6367, $R^2 = 0.88$). These improved results were attributed to suppress of nonspecific binding with BSA. .

Before applying SERS dots to immunoassay, the assay condition for removal of nonspecific binding during the last step of forming on-chip

sandwich-immunocomplexes was confirmed (Figure 3-8). We observed that the degree of nonspecific bindings was dependent on the concentrations of SERS dot and was effectively suppressed when concentration of SERS dot solution containing BSA was below than 0.5 mg/mL (Figure 3-8c). Thus, applying 0.25 mg/mL SERS dot solution containing 1*w/w* % BSA to immunoassay was expected to offer an effective reducing of nonspecific binding.

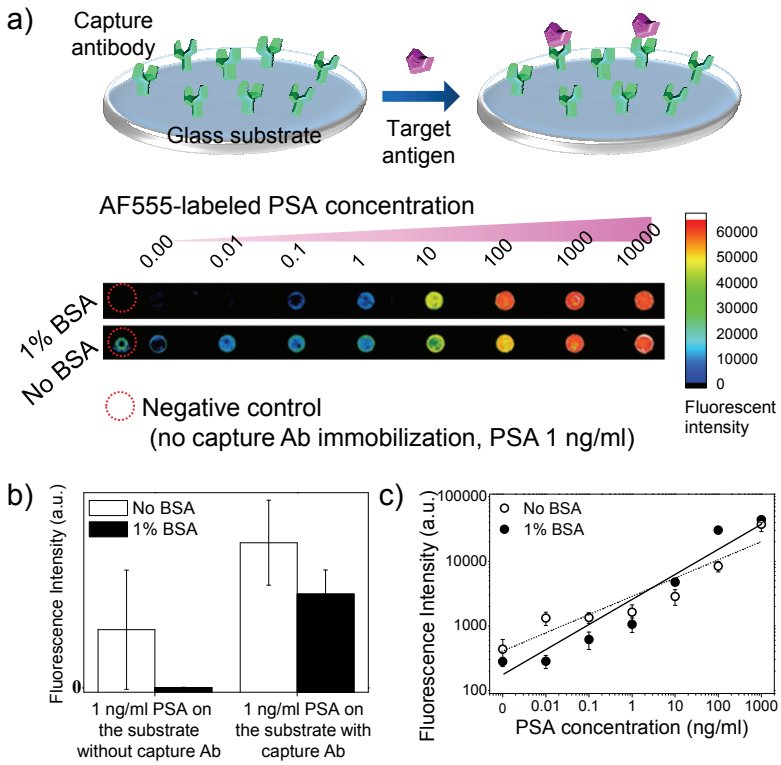

Figure 3-7. Capturing of target antigen (PSA) on the anti-PSA antibody immobilized-substrate.

Relative amount of captured target antigen was determined by fluorescence intensity of Alexafluor®555-labeled PSA. (a) Fluorescence scanning image of spot-arrayed slide with different PSA conjugation buffer condition (containing 1% BSA or not). (b) Blocking effect of BSA to nonspecific binding. Two types of substrate (the capture antibody immobilized and the no capture antibody immobilized) were used. Antigen concentration was 1 ng/mL. (c) Analysis of fluorescence intensity with increasing PSA concentration.

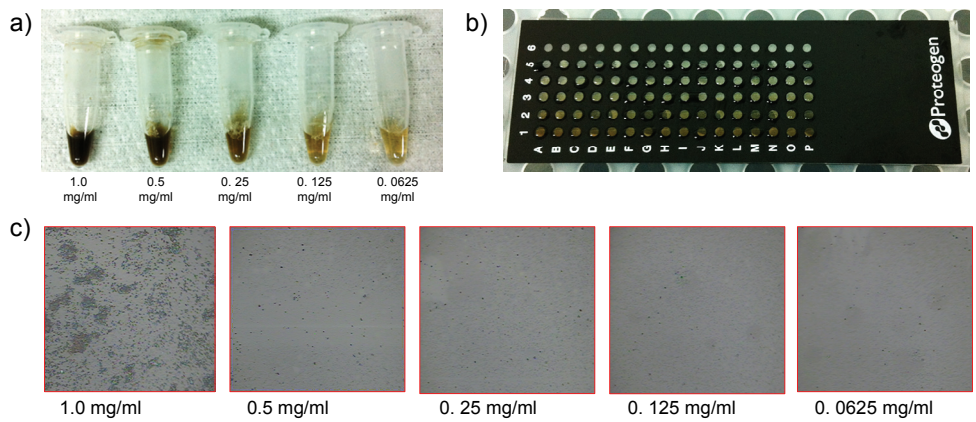

Figure 3-8. Photographs of SERS dot solutions and the concentration dependence of non-specific binding.

(a) The photograph of SERS dot solution of different concentrations (1, 0.5, 0.25, 0.125, 0.0625 mg/mL). (b) The photograph of spot-arrayed glass slide during incubation of SERS dot solutions. (c) The representative optical images of the chip surfaces showing non-specific binding levels. The images were obtained on 0 ng/mL of PSA (control) spots after incubation of different SERS dot concentration solutions and washing.

2. 4. Evaluation of SERS-based Immunoassays

PSA as a biomarker of prostate cancer was used for validation of the immunoassay platform. PSA at 0.001−1000 ng/mL was incubated on the capture substrate (Figure 3-9), followed by incubation with tracer antibody-conjugated SERS $dot_{4\text{-}FBT}$ to enable selective tagging of captured PSAs. After forming sandwich complexes, SERS intensities were measured using Raman spectroscopy. The SERS spectra from each sample were measured by scanning the areas of 200 × 200 μm^2, followed by averaging of triplicates. As shown in Figure 3-10a (inset), unique bands of SERS $dots_{4\text{-}FBT}$ (386, 623, 814 and 1075 cm^{-1}) were evident, the intensities of which increased with increasing PSA concentration. A standard calibration curve was obtained by plotting the intensity of 386 cm^{-1} band as a function of the logarithm of PSA concentration (Figure 3-10a), exhibiting a wide dynamic range of 0.001−1000 ng/mL. The plot exhibited strong linearity (R^2 = 0.997) over five orders of magnitude below 10 ng/mL PSA. An assay platform that yields consistent results at low and high concentrations is useful in terms of integration of tools for diagnosis and monitoring of disease status. The limit of detection (LOD), defined as the analyte concentration that produces a signal threefold higher than the standard deviation of blank measurements (162 in this experiment), was 0.11 pg/mL. This suggests a much wider dynamic range with lower LOD compared to a recently reported enzyme-linked immunosorbent assay for PSA.[96]

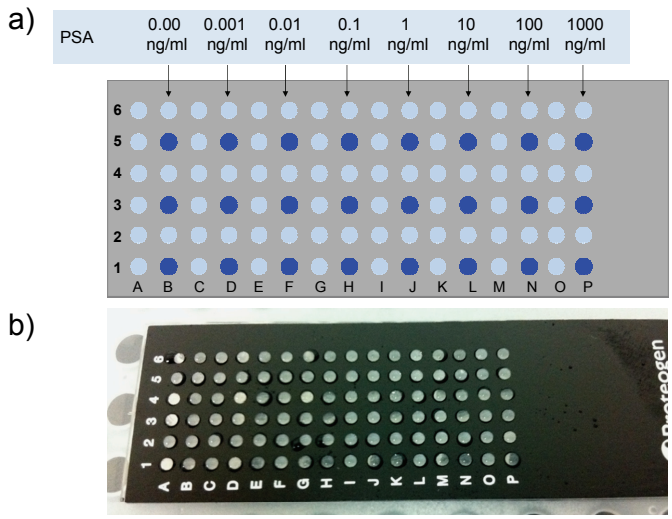

Figure 3-9. Incubation concentration of PSA on a spot-arrayed glass slide.

(a) Schematic illustration and (b) the photograph of a spot-arrayed glass slide.

Table 3-1. SERS intensity of standard samples (in Figure 3-10a)

PSA (pg/mL)	SERS Intensity (a.u.)	
	Mean	Standard deviation
Blanck	229.7	161.9
10^0	3617.6	335.1
10^1	9582.4	3038.5
10^2	14730.9	2928.6
10^3	21668.5	1140.1
10^4	30908.5	4708.6
10^5	52260.0	3938.3
10^6	88161.8	5903.9

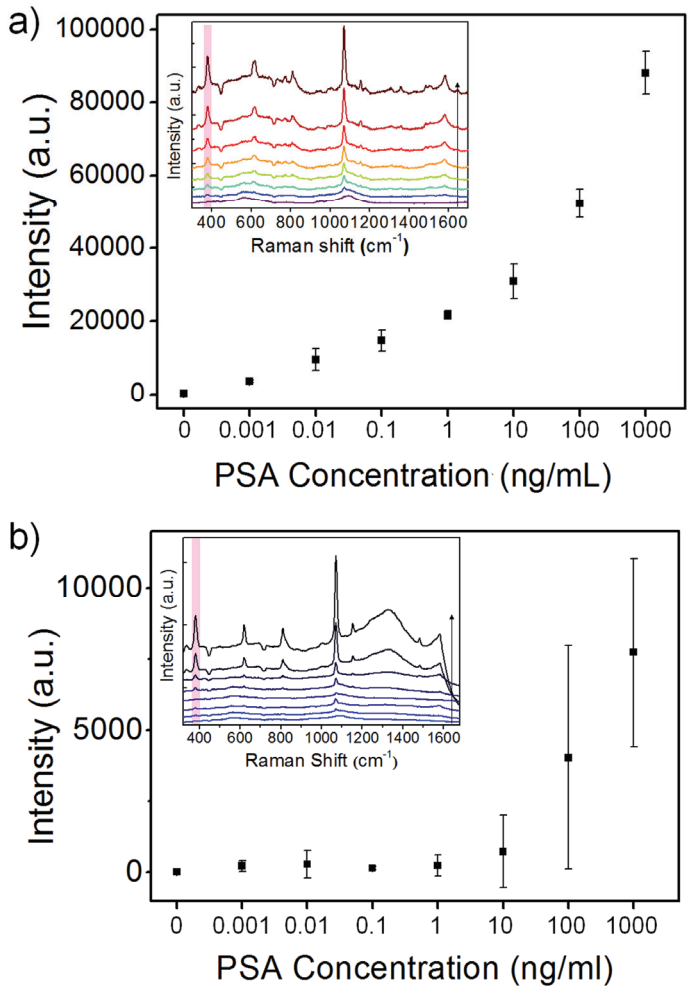

Figure 3-10. PSA immunoassay results using SERS dot$_{4\text{-FBT}}$

Each one is obtained by (a) the Raman area-scanning method, and (b) a conventional Raman mapping method for comparision. Dose-response relations on a semi-log scale were obtained by quantifying the 386 cm^{-1} band intensities of 4-FBT. Insets show SERS spectra of SERS dot$_{4\text{-FBT}}$ at PSA concentrations of 0 and 0.001–1000 ng/mL.

We interpret that sensitivity could be enhanced using SERS dots and a full-area rapid readout platform. This system allowed a 1,000-fold more rapid measurement and 2.5-fold higher sensitivity than the point-scanning method.[78] For comparison, the immunoassay result was also obtained by conventional point-by-point mapping manner (Figure 3-10b). Average spectra over 10 × 10 point mapping with 10 μm-step size and an acquisition time of 1 s/point (total, 100 s) from each array spot were obtained, and then the results of triplicate determinations averaged to attain the final spectra, and the intensities of SERS dot4-FBT (386 cm^{-1} band) were plotted against PSA concentration (Figure 3-10b). This measurement was performed using conditions identical to those for full area-scanning readout (e.g. same acquisition time, laser power, etc.). The LOD and dynamic range of the conventional point-by-point mapping assay were 0.1–1 ng/mL and 1–1000 ng/mL, respectively (Figure 3-11). These results indicate that full-area readout enhances the sensitivity and dynamic range of chip-based immunoassays.

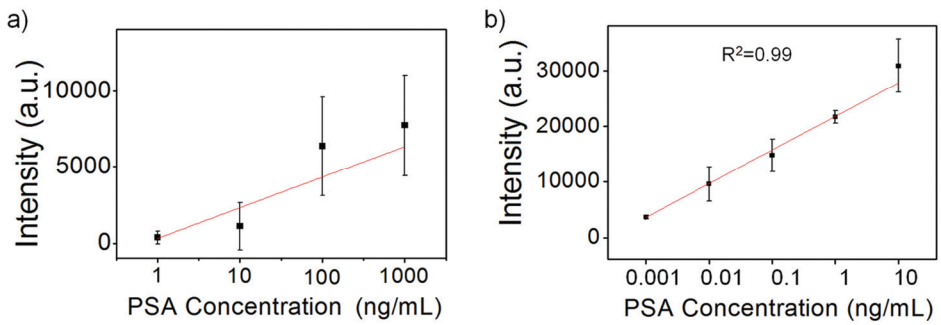

Figure 3-11. Dose-response curves of PSA immunoassay with fitting curve in linear range

Wtih the same assay protocol, different results were obtained from (a) conventional Raman mapping method and (b) Raman area-scanning method.

In addition, we performed comparative experiments using commercial immunoassay kits, such as immunoradiometric assay (IRMA) and chemiluminescence immunoassay (CLIA), which are used clinically for diagnosis (Figure 3-12). Although the LODs of the IRMA and CLIA methods were 31 and 66 pg/mL, respectively, both methods exhibited poor linearity at <0.1 ng/mL PSA. In contrast, our SERS immunoassay had a lower LOD and good linearity. Therefore, our SIA can be said to detect PSA with higher sensitivity and a wider dynamic range due to the combination of the ensemble averaged signals of single SERS dot particles and the area-scanning readout method.

Finally, we adopted the platform to detect PSA in a patient's serum (Figure 3-13). The patient's serum sample (C_0) was serially diluted into solutions of concentration ranging from $1/2 \cdot C_0$ to $1E\text{-}4 \cdot C_0$ and its PSA concentration was measured by our SIA platform. The correlation coefficient (R^2) of the measured PSA level with the expected value from IRMA was 0.9899, and this result reveals that the LOD of serum sample is also below 4 pg/mL.

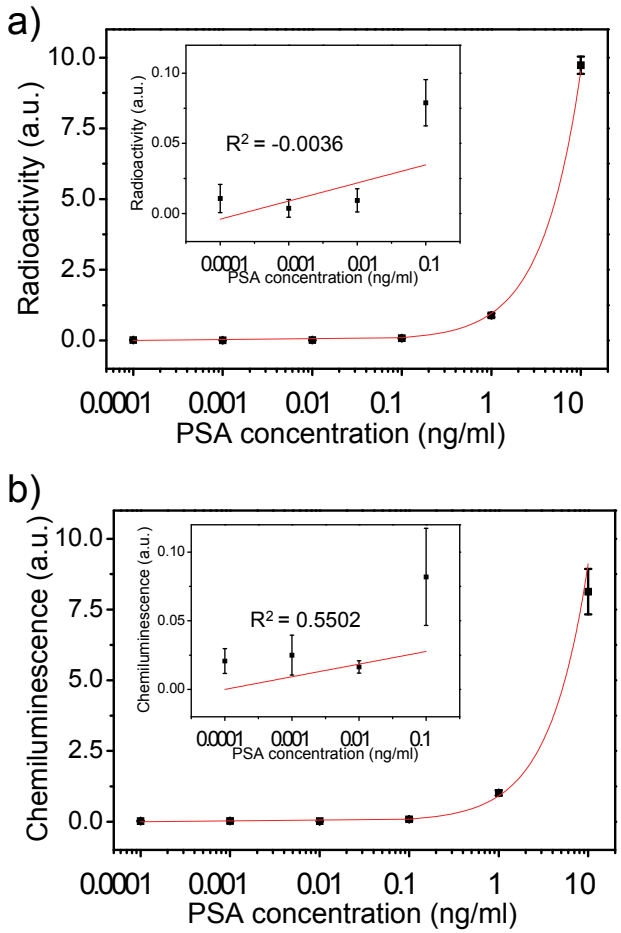

Figure 3-12. Comparison with commercial assay protocols.

(a) Immunoradiometric assay (IRMA) results for PSA analysis. Radioactivity intensities in the PSA concentration range of 0.0001 – 10 ng/mL, and 0.0001 – 0.1 ng/mL (inset) for linear fitting. (b) Chemiluminescence immunoassay (CLIA) results for PSA analysis. Chemiluminescence intensities in the PSA concentration range of 0.0001 – 10 ng/mL, and 0.0001 – 0.1 ng/mL (inset) for linear plot.

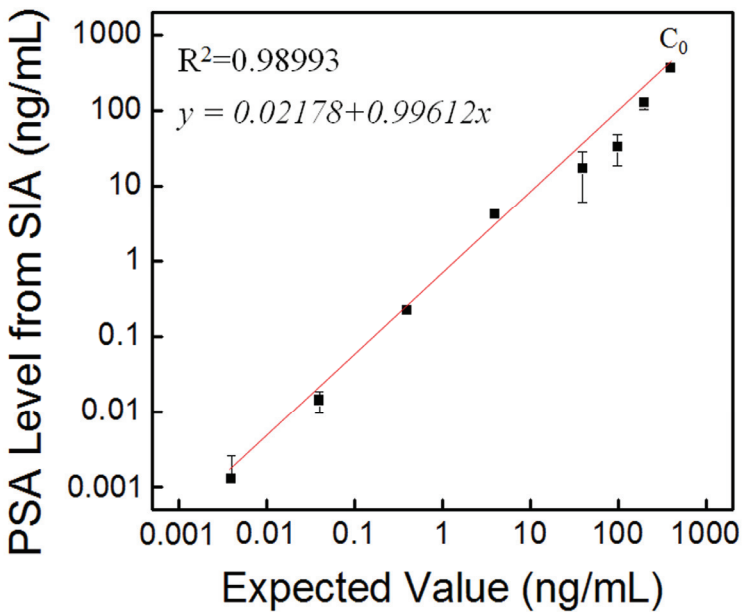

Figure 3-13. Correlation of PSA level measured from SIA with expected value from a patient's serum sample.

The patient's serum (highest concentration point, C_0) was serially diluted with PBS containing 1% BSA, and their PSA levels were evaluated by SIA. The C_0 value was measured as 399 ng/mL from IRMA, and the expected values were calculated from the dilution factor of each sample.

Conclusion

In summary, we demonstrated a sensitive SERS-based immunoassay (SIA) using SERS active nanoparticles and a full-area rastering confocal Raman readout method.

For development multiplexed and quantifiable SERS nanoprobes, first, we constructed a heterometallic SERS probe based on a silver shell and gold NPs, affording highly uniform and strong SERS activity. The Ag-Au SS structures exhibited a red-shift of plasmonic resonance band to the NIR region with highly enhanced SERS signals (SERS enhancement factor: ~1.4 $\times$ 10^6 with 11% relative standard deviation) and reproducibility (100% detectable) by the 785-nm photoexcitation. These outstanding SERS activities were independent of the laser polarizations and largely attributed to the 3-D distribution of SERS hot spots between the Ag shell and the satellite particles on it. Finally, we demonstrated Ag-Au SS as NIR SERS probes through proof-of-concept of *in vivo* imaging application.

Second, we investigated different readout methods suitable for quantitative bioassays based on SERS probes. Sample survey measurement approach revealed intensity fluctuation due to inherent heterogeneity of particle distributions and statistical limitation whereas utilization of enlarged FOV increased noise signals due to increased collection depth through the chip substrate. On the basis of these results, a new readout

method for chip-based immunoassay using SERS nanoprobes was designed and validated. This method adopted raster scan over an entire chip area with confocal mode while accumulating signals in a CCD detector to obtain a single spectrum per frame. This method demonstrated a 1,000 times fast scanning holding complete survey advantage while sacrificing 2.5 times sensitivity. The idea benefits also commercially available Raman systems (e.g. DuoScan®, JY-HORIBA) which use dual galvo-mirrors to scan the excitation light over a large 2D surface and accumulate signals in a single spectrum. We expect that this microscope-based readout method could serve successfully as a tool for bioassays using SERS probes.

Lastly using SERS dots, which are sufficiently sensitive and photostable to be detected at the single probe level, we developed a novel SIA protocols. The SERS dots were conjugated with a tracer antibody and evaluated in terms of bio-functionality. The antibody conjugated SERS dots exhibited specificity and selectivity. As a capture substrate, glass slide was utilized, and the incubation coditions on chip were investigated successfully using fluorescence labeled antibody. Flinally, with all the developed protocols, PSA could be detected with a sensitivity of ~0.11 pg/mL and a dynamic range of 5 orders of magnitude due to the self-bright SERS probe and the whole area-scanning readout method. We could adopt this SIA platforms to

detect PSA in patiant's samples. This represents a powerful, inexpensive, and rapid multiplex immunoassay platform with high sensitivity and reliability over a wide dynamic range.

References

(1) Zhu, X.; Xu, T.; Lin, Q.; Duan, Y. Technical Development of Raman Spectroscopy: From Instrumental to Advanced Combined Technologies. *Appl. Spectrosc. Rev.* **2013,** *49*, 64-82.

(2) Moskovits, M. Surface-enhanced spectroscopy. *Rev. Mod. Phys.* **1985,** *57*, 783-826.

(3) Fleischmann, M.; Hendra, P. J.; McQuillan, A. J. Raman spectra of pyridine adsorbed at a silver electrode. *Chem. Phys. Lett.* **1974,** *26*, 163-166.

(4) Campion, A.; Kambhampati, P. Surface-enhanced Raman scattering. *Chem. Soc. Rev.* **1998,** *27*, 241-250.

(5) Jun, B. H.; Kim, G.; Noh, M. S.; Kang, H.; Kim, Y. K.; Cho, M. H.; Jeong, D. H.; Lee, Y.-S. Surface-enhanced Raman scattering-active nanostructures and strategies for bioassays. *Nanomedicine* **2011,** *6*, 1463-1480.

(6) Schlucker, S. SERS microscopy: nanoparticle probes and biomedical applications. *ChemPhysChem* **2009,** *10*, 1344-1354.

(7) Schlucker, S. Surface-enhanced Raman spectroscopy: concepts and chemical applications. *Angew. Chem., Int. Ed.* **2014,** *53*, 4756-4795.

(8) Wang, Y.; Yan, B.; Chen, L. SERS tags: novel optical nanoprobes for bioanalysis. *Chem. Rev.* **2013,** *113*, 1391-1428.

(9) Lee, H. E.; Lee, H. K.; Chang, H.; Ahn, H. Y.; Erdene, N.; Lee, H. Y.; Lee, Y.-S.; Jeong, D. H.; Chung, J.; Nam, K. T. Virus templated gold nanocube chain for SERS nanoprobe. *Small* **2014,** *10*, 3007-3011.

(10) Guarrotxena, N.; Bazan, G. C. Antitags: SERS-encoded nanoparticle assemblies that enable single-spot multiplex protein detection. *Adv. Mater.* **2014,** *26*, 1941-1946.

(11) Lee, J. H.; Nam, J. M.; Jeon, K. S.; Lim, D. K.; Kim, H.; Kwon, S.; Lee, H.; Suh, Y. D. Tuning and maximizing the single-molecule surface-enhanced Raman scattering from DNA-tethered nanodumbbells. *ACS Nano* **2012,** *6*, 9574-9584.

(12) Chon, H.; Lee, S.; Son, S. W.; Oh, C. H.; Choo, J. Highly sensitive immunoassay of lung cancer marker carcinoembryonic antigen using surface-enhanced Raman scattering of hollow gold nanospheres. *Anal. Chem.* **2009,** *81*, 3029-3034.

(13) Kang, H.; Jeong, S.; Koh, Y.; Geun Cha, M.; Yang, J. K.; Kyeong, S.; Kim, J.; Kwak, S. Y.; Chang, H. J.; Lee, H.; Jeong, C.; Kim, J. H.; Jun, B. H.; Kim, Y. K.; Hong Jeong, D.; Lee, Y. S. Direct identification of on-bead peptides using surface-enhanced Raman spectroscopic barcoding system for high-throughput bioanalysis. *Sci. Rep.* **2015,** *5*, 10144.

(14) Salehi, M.; Schneider, L.; Strobel, P.; Marx, A.; Packeisen, J.; Schlücker, S. Two-color SERS microscopy for protein co-localization in prostate tissue with primary antibody-protein A/G-gold nanocluster conjugates. *Nanoscale* **2014,** *6*, 2361-2367.

(15) Wang, G.; Park, H. Y.; Lipert, R. J.; Porter, M. D. Mixed monolayers on gold nanoparticle labels for multiplexed surface-enhanced Raman scattering based immunoassays. *Anal. Chem.* **2009,** *81*, 9643-9650.

(16) Alvarez-Puebla, R. A.; Liz-Marzan, L. M. SERS-based diagnosis and biodetection. *Small* **2010,** *6*, 604-610.

(17) Kang, H.; Yang, J.-K.; Noh, M. S.; Jo, A.; Jeong, S.; Lee, M.; Lee, S.; Chang, H.; Lee, H.; Jeon, S.-J.; Kim, H.-I.; Cho, M.-H.; Lee, H.-Y.; Kim, J.-H.; Jeong, D. H.; Lee, Y.-S. One-step synthesis of silver nanoshells with bumps for highly sensitive near-IR SERS nanoprobes. *J. Mater. Chem. B*

2014, *2*, 4415-4421.

(18) Kang, H.; Jeong, S.; Park, Y.; Yim, J.; Jun, B.-H.; Kyeong, S.; Yang, J.-K.; Kim, G.; Hong, S.; Lee, L. P.; Kim, J.-H.; Lee, H.-Y.; Jeong, D. H.; Lee, Y.-S. Near-Infrared SERS Nanoprobes with Plasmonic Au/Ag Hollow-Shell Assemblies for In Vivo Multiplex Detection. *Adv. Funct. Mater.* **2013,** *23*, 3719-3727.

(19) Wang, G.; Lipert, R. J.; Jain, M.; Kaur, S.; Chakraboty, S.; Torres, M. P.; Batra, S. K.; Brand, R. E.; Porter, M. D. Detection of the potential pancreatic cancer marker MUC4 in serum using surface-enhanced Raman scattering. *Anal. Chem.* **2011,** *83*, 2554-2561.

(20) Park, H.; Lee, S.; Chen, L.; Lee, E. K.; Shin, S. Y.; Lee, Y. H.; Son, S. W.; Oh, C. H.; Song, J. M.; Kang, S. H.; Choo, J. SERS imaging of HER2-overexpressed MCF7 cells using antibody-conjugated gold nanorods. *Phys. Chem. Chem. Phys.* **2009,** *11*, 7444-7449.

(21) Sun, L.; Sung, K. B.; Dentinger, C.; Lutz, B.; Nguyen, L.; Zhang, J.; Qin, H.; Yamakawa, M.; Cao, M.; Lu, Y.; Chmura, A. J.; Zhu, J.; Su, X.; Berlin, A. A.; Chan, S.; Knudsen, B. Composite organic-inorganic nanoparticles as Raman labels for tissue analysis. *Nano Lett.* **2007,** *7*, 351-

356.

(22) Lin, L.; Gu, H.; Ye, J. Plasmonic multi-shell nanomatryoshka particles as highly tunable SERS tags with built-in reporters. *Chem. Commun.* **2015,** *51*, 17740-17743.

(23) Lim, D. K.; Jeon, K. S.; Hwang, J. H.; Kim, H.; Kwon, S.; Suh, Y. D.; Nam, J. M. Highly uniform and reproducible surface-enhanced Raman scattering from DNA-tailorable nanoparticles with 1-nm interior gap. *Nat. Nanotechnol.* **2011,** *6*, 452-460.

(24) Nie, S. Probing Single Molecules and Single Nanoparticles by Surface-Enhanced Raman Scattering. *Science* **1997,** *275*, 1102-1106.

(25) Kneipp, K.; Wang, Y.; Kneipp, H.; Perelman, L. T.; Itzkan, I.; Dasari, R. R.; Feld, M. S. Single Molecule Detection Using Surface-Enhanced Raman Scattering (SERS). *Phys. Rev. Lett.* **1997,** *78*, 1667-1670.

(26) Lim, D. K.; Jeon, K. S.; Kim, H. M.; Nam, J. M.; Suh, Y. D. Nanogap-engineerable Raman-active nanodumbbells for single-molecule detection. *Nat. Mater.* **2010,** *9*, 60-67.

(27) Li, J. F.; Huang, Y. F.; Ding, Y.; Yang, Z. L.; Li, S. B.; Zhou, X. S.; Fan, F. R.; Zhang, W.; Zhou, Z. Y.; Wu de, Y.; Ren, B.; Wang, Z. L.; Tian,

Z. Q. Shell-isolated nanoparticle-enhanced Raman spectroscopy. *Nature* **2010,** *464*, 392-395.

(28) Shafer-Peltier, K. E.; Haynes, C. L.; Glucksberg, M. R.; Van Duyne, R. P. Toward a glucose biosensor based on surface-enhanced Raman scattering. *J. Am. Chem. Soc.* **2003,** *125*, 588-593.

(29) Qian, X.; Peng, X. H.; Ansari, D. O.; Yin-Goen, Q.; Chen, G. Z.; Shin, D. M.; Yang, L.; Young, A. N.; Wang, M. D.; Nie, S. In vivo tumor targeting and spectroscopic detection with surface-enhanced Raman nanoparticle tags. *Nat. Biotechnol.* **2008,** *26*, 83-90.

(30) Jun, B. H.; Noh, M. S.; Kim, J.; Kim, G.; Kang, H.; Kim, M. S.; Seo, Y. T.; Baek, J.; Kim, J. H.; Park, J.; Kim, S.; Kim, Y. K.; Hyeon, T.; Cho, M. H.; Jeong, D. H.; Lee, Y. S. Multifunctional silver-embedded magnetic nanoparticles as SERS nanoprobes and their applications. *Small* **2010,** *6*, 119-125.

(31) Yu, K. N.; Lee, S. M.; Han, J. Y.; Park, H.; Woo, M. A.; Noh, M. S.; Hwang, S. K.; Kwon, J. T.; Jin, H.; Kim, Y. K.; Hergenrother, P. J.; Jeong, D. H.; Lee, Y. S.; Cho, M. H. Multiplex targeting, tracking, and imaging of apoptosis by fluorescent surface enhanced Raman spectroscopic dots.

Bioconjug Chem **2007,** *18*, 1155-1162.

(32) Kim, J. H.; Kim, J. S.; Choi, H.; Lee, S. M.; Jun, B. H.; Yu, K. N.; Kuk, E.; Kim, Y. K.; Jeong, D. H.; Cho, M. H.; Lee, Y.-S. Nanoparticle probes with surface enhanced Raman spectroscopic tags for cellular cancer targeting. *Anal. Chem.* **2006,** *78*, 6967-6973.

(33) Su, X.; Zhang, J.; Sun, L.; Koo, T. W.; Chan, S.; Sundararajan, N.; Yamakawa, M.; Berlin, A. A. Composite organic-inorganic nanoparticles (COINs) with chemically encoded optical signatures. *Nano Lett.* **2005,** *5*, 49-54.

(34) Grubisha, D. S.; Lipert, R. J.; Park, H. Y.; Driskell, J.; Porter, M. D. Femtomolar detection of prostate-specific antigen: an immunoassay based on surface-enhanced Raman scattering and immunogold labels. *Anal. Chem.* **2003,** *75*, 5936-5943.

(35) Gellner, M.; Steinigeweg, D.; Ichilmann, S.; Salehi, M.; Schutz, M.; Kompe, K.; Haase, M.; Schlucker, S. 3D self-assembled plasmonic superstructures of gold nanospheres: synthesis and characterization at the single-particle level. *Small* **2011,** *7*, 3445-3451.

(36) Yoon, J. H.; Lim, J.; Yoon, S. Controlled assembly and plasmonic

properties of asymmetric core-satellite nanoassemblies. *ACS Nano* **2012,** *6*, 7199-7208.

(37) Xu, L.; Kuang, H.; Xu, C.; Ma, W.; Wang, L.; Kotov, N. A. Regiospecific plasmonic assemblies for in situ Raman spectroscopy in live cells. *J. Am. Chem. Soc.* **2012,** *134*, 1699-1709.

(38) Gandra, N.; Singamaneni, S. "Clicked" plasmonic core-satellites: covalently assembled gold nanoparticles. *Chem. Commun.* **2012,** *48*, 11540-11542.

(39) Gandra, N.; Abbas, A.; Tian, L.; Singamaneni, S. Plasmonic planet-satellite analogues: hierarchical self-assembly of gold nanostructures. *Nano Lett.* **2012,** *12*, 2645-2651.

(40) Rodríguez-Lorenzo, L.; Álvarez-Puebla, R. n. A.; de Abajo, F. J. G. a.; Liz-Marzán, L. M. Surface Enhanced Raman Scattering Using Star-Shaped Gold Colloidal Nanoparticles. *J. Phy. Chem. C* **2010,** *114*, 7336-7340.

(41) Mulvihill, M. J.; Ling, X. Y.; Henzie, J.; Yang, P. Anisotropic etching of silver nanoparticles for plasmonic structures capable of single-particle SERS. *J. Am. Chem. Soc.* **2010,** *132*, 268-274.

(42) Samanta, A.; Jana, S.; Das, R. K.; Chang, Y.-T. Wavelength and shape dependent SERS study to develop ultrasensitive nanotags for imaging of cancer cells. *RSC Advances* **2014,** *4*, 12415-12421.

(43) Samanta, A.; Maiti, K. K.; Soh, K.-S.; Liao, X.; Vendrell, M.; Dinish, U. S.; Yun, S.-W.; Bhuvaneswari, R.; Kim, H.; Rautela, S.; Chung, J.; Olivo, M.; Chang, Y.-T. Ultrasensitive Near-Infrared Raman Reporters for SERS-Based In Vivo Cancer Detection. *Angew. Chem., Int. Ed.* **2011,** *123*, 6213-6216.

(44) Cho, S. J.; Ahn, Y. H.; Maiti, K. K.; Dinish, U. S.; Fu, C. Y.; Thoniyot, P.; Olivo, M.; Chang, Y. T. Combinatorial synthesis of a triphenylmethine library and their application in the development of surface enhanced Raman scattering (SERS) probes. *Chem. Commun.* **2010,** *46*, 722-724.

(45) Guerrini, L.; Graham, D. Molecularly-mediated assemblies of plasmonic nanoparticles for Surface-Enhanced Raman Spectroscopy applications. *Chem. Soc. Rev.* **2012,** *41*, 7085-7107.

(46) Li, W.; Camargo, P. H.; Lu, X.; Xia, Y. Dimers of silver nanospheres: facile synthesis and their use as hot spots for surface-enhanced Raman

scattering. *Nano Lett.* **2009,** *9*, 485-490.

(47) Braun, G. B.; Lee, S. J.; Laurence, T.; Fera, N.; Fabris, L.; Bazan, G. C.; Moskovits, M.; Reich, N. O. Generalized Approach to SERS-Active Nanomaterials via Controlled Nanoparticle Linking, Polymer Encapsulation, and Small-Molecule Infusion. *J. Phy. Chem. C* **2009,** *113*, 13622-13629.

(48) Guarrotxena, N.; Liu, B.; Fabris, L.; Bazan, G. C. Antitags: nanostructured tools for developing SERS-based ELISA analogs. *Adv. Mater.* **2010,** *22*, 4954-4958.

(49) Yigit, M. V.; Zhu, L.; Ifediba, M. A.; Zhang, Y.; Carr, K.; Moore, A.; Medarova, Z. Noninvasive MRI-SERS imaging in living mice using an innately bimodal nanomaterial. *ACS Nano* **2011,** *5*, 1056-1066.

(50) Brown, L. O.; Doorn, S. K. A controlled and reproducible pathway to dye-tagged, encapsulated silver nanoparticles as substrates for SERS multiplexing. *Langmuir* **2008,** *24*, 2277-2280.

(51) Fang, Y.; Seong, N.-H.; Dlott, D. D. Measurement of the Distribution of Site Enhancements in Surface-Enhanced Raman Scattering. *Science* **2008,** *321*, 388-392.

(52) Lal, S.; Link, S.; Halas, N. J. Nano-optics from sensing to waveguiding. *Nat. Photonics* **2007,** *1*, 641-648.

(53) Xu, L.; Hao, C.; Yin, H.; Liu, L.; Ma, W.; Wang, L.; Kuang, H.; Xu, C. Plasmonic Core-Satellites Nanostructures with High Chirality and Bioproperty. *J. Phys. Chem. Lett.* **2013,** *4*, 2379-2384.

(54) Chen, S.-Y.; Lazarides, A. A. Quantitative Amplification of Cy5 SERS in 'Warm Spots' Created by Plasmonic Coupling in Nanoparticle Assemblies of Controlled Structure†. *J. Phy. Chem. C* **2009,** *113*, 12167-12175.

(55) Smith, B. R.; Zavaleta, C.; Rosenberg, J.; Tong, R.; Ramunas, J.; Liu, Z.; Dai, H.; Gambhir, S. S. High-resolution, serial intravital microscopic imaging of nanoparticle delivery and targeting in a small animal tumor model. *Nano today* **2013,** *8*, 126-137.

(56) Ghosh, D.; Lee, Y.; Thomas, S.; Kohli, A. G.; Yun, D. S.; Belcher, A. M.; Kelly, K. A. M13-templated magnetic nanoparticles for targeted in vivo imaging of prostate cancer. *Nat. Nanotechnol.* **2012,** *7*, 677-682.

(57) Jeong, H. H.; Erdene, N.; Park, J. H.; Jeong, D. H.; Lee, H. Y.; Lee, S. K. Real-time label-free immunoassay of interferon-gamma and prostate-

specific antigen using a Fiber-Optic Localized Surface Plasmon Resonance sensor. *Biosens. Bioelectron.* **2013,** *39*, 346-351.

(58) Chon, H.; Lee, S.; Yoon, S. Y.; Lee, E. K.; Chang, S. I.; Choo, J. SERS-based competitive immunoassay of troponin I and CK-MB markers for early diagnosis of acute myocardial infarction. *Chem. Commun.* **2014,** *50*, 1058-1060.

(59) Wang, K. Y.; Chuang, S. A.; Lin, P. C.; Huang, L. S.; Chen, S. H.; Ouarda, S.; Pan, W. H.; Lee, P. Y.; Lin, C. C.; Chen, Y. J. Multiplexed immunoassay: quantitation and profiling of serum biomarkers using magnetic nanoprobes and MALDI-TOF MS. *Anal. Chem.* **2008,** *80*, 6159-6167.

(60) Lang, Q.; Wang, F.; Yin, L.; Liu, M.; Petrenko, V. A.; Liu, A. Specific probe selection from landscape phage display library and its application in enzyme-linked immunosorbent assay of free prostate-specific antigen. *Anal. Chem.* **2014,** *86*, 2767-2774.

(61) Gu, B.; Xu, C.; Yang, C.; Liu, S.; Wang, M. ZnO quantum dot labeled immunosensor for carbohydrate antigen 19-9. *Biosens. Bioelectron.* **2011,** *26*, 2720-2723.

(62) Rusling, J. F. Multiplexed electrochemical protein detection and translation to personalized cancer diagnostics. *Anal. Chem.* **2013,** *85*, 5304-5310.

(63) Narayanan, R.; Lipert, R. J.; Porter, M. D. Cetyltrimethylammonium bromide-modified spherical and cube-like gold nanoparticles as extrinsic Raman labels in surface-enhanced Raman spectroscopy based heterogeneous immunoassays. *Anal. Chem.* **2008,** *80*, 2265-2271.

(64) Liang, J.; Liu, H.; Huang, C.; Yao, C.; Fu, Q.; Li, X.; Cao, D.; Luo, Z.; Tang, Y. Aggregated silver nanoparticles based surface-enhanced Raman scattering enzyme-linked immunosorbent assay for ultrasensitive detection of protein biomarkers and small molecules. *Anal. Chem.* **2015,** *87*, 5790-5796.

(65) Li, M.; Kang, J. W.; Sukumar, S.; Dasari, R. R.; Barman, I. Multiplexed detection of serological cancer markers with plasmon-enhanced Raman spectro-immunoassay. *Chem. Sci.* **2015,** *6*, 3906-3914.

(66) Driskell, J. D.; Kwarta, K. M.; Lipert, R. J.; Porter, M. D.; Neill, J. D.; Ridpath, J. F. Low-level detection of viral pathogens by a surface-enhanced Raman scattering based immunoassay. *Anal. Chem.* **2005,** *77*,

6147-6154.

(67) Gao, R.; Cheng, Z.; deMello, A. J.; Choo, J. Wash-free magnetic immunoassay of the PSA cancer marker using SERS and droplet microfluidics. *Lab Chip* **2016,** *16*, 1022-1029.

(68) Kang, T.; Yoo, S. M.; Yoon, I.; Lee, S. Y.; Kim, B. Patterned multiplex pathogen DNA detection by Au particle-on-wire SERS sensor. *Nano Lett.* **2010,** *10*, 1189-1193.

(69) Kim, H. I.; Hwang, D.; Jeon, S. J.; Lee, S.; Park, J. H.; Yim, D.; Yang, J. K.; Kang, H.; Choo, J.; Lee, Y. S.; Chung, J.; Kim, J. H. Orientation and density control of bispecific anti-HER2 antibody on functionalized carbon nanotubes for amplifying effective binding reactivity to cancer cells. *Nanoscale* **2015,** *7*, 6363-6373.

(70) Henry, N. L.; Hayes, D. F. Cancer biomarkers. *Mol. Oncol.* **2012,** *6*, 140-146.

(71) Granger, J. H.; Granger, M. C.; Firpo, M. A.; Mulvihill, S. J.; Porter, M. D. Toward development of a surface-enhanced Raman scattering (SERS)-based cancer diagnostic immunoassay panel. *Analyst* **2013,** *138*, 410-416.

(72) Wang, Y.; Salehi, M.; Schutz, M.; Schlücker, S. Femtogram detection of cytokines in a direct dot-blot assay using SERS microspectroscopy and hydrophilically stabilized Au-Ag nanoshells. *Chem. Commun.* **2014,** *50*, 2711-2714.

(73) Lee, M.; Lee, S.; Lee, J. H.; Lim, H. W.; Seong, G. H.; Lee, E. K.; Chang, S. I.; Oh, C. H.; Choo, J. Highly reproducible immunoassay of cancer markers on a gold-patterned microarray chip using surface-enhanced Raman scattering imaging. *Biosens. Bioelectron.* **2011,** *26*, 2135-2141.

(74) Thaxton, C. S.; Elghanian, R.; Thomas, A. D.; Stoeva, S. I.; Lee, J. S.; Smith, N. D.; Schaeffer, A. J.; Klocker, H.; Horninger, W.; Bartsch, G.; Mirkin, C. A. Nanoparticle-based bio-barcode assay redefines "undetectable" PSA and biochemical recurrence after radical prostatectomy. *Proc. Natl. Acad. Sci. U. S. A.* **2009,** *106*, 18437-18442.

(75) De Angelis, G.; Rittenhouse, H. G.; Mikolajczyk, S. D.; Blair Shamel, L.; Semjonow, A. Twenty Years of PSA: From Prostate Antigen to Tumor Marker. *Rev. Urol.* **2007,** *9*, 113-123.

(76) Zavaleta, C. L.; Smith, B. R.; Walton, I.; Doering, W.; Davis, G.;

Shojaei, B.; Natan, M. J.; Gambhir, S. S. Multiplexed imaging of surface enhanced Raman scattering nanotags in living mice using noninvasive Raman spectroscopy. *Proc. Natl. Acad. Sci. U. S. A.* **2009,** *106*, 13511-13516.

(77) Kircher, M. F.; de la Zerda, A.; Jokerst, J. V.; Zavaleta, C. L.; Kempen, P. J.; Mittra, E.; Pitter, K.; Huang, R.; Campos, C.; Habte, F.; Sinclair, R.; Brennan, C. W.; Mellinghoff, I. K.; Holland, E. C.; Gambhir, S. S. A brain tumor molecular imaging strategy using a new triple-modality MRI-photoacoustic-Raman nanoparticle. *Nat. Med.* **2012,** *18*, 829-834.

(78) Chang, H.; Kang, H.; Jeong, S.; Ko, E.; Lee, Y.-S.; Lee, H.-Y.; Jeong, D. H. A fast and reliable readout method for quantitative analysis of surface-enhanced Raman scattering nanoprobes on chip surface. *Rev. Sci. Instrum.* **2015,** *86*, 055004.

(79) Kim, J. H.; Kang, H.; Kim, S.; Jun, B. H.; Kang, T.; Chae, J.; Jeong, S.; Kim, J.; Jeong, D. H.; Lee, Y.-S. Encoding peptide sequences with surface-enhanced Raman spectroscopic nanoparticles. *Chem. Commun.* **2011,** *47*, 2306-2308.

(80) Stöber, W.; Fink, A.; Bohn, E. Controlled Growth of Monodispersed Silica Sphere in the Micron Size Range. *J. Colloid Interface Sci.* **1968,** *26*, 62-69.

(81) Kang, H.; Kang, T.; Kim, S.; Kim, J.-H.; Jun, B.-H.; Chae, J.; Park, J.; Jeong, D. H.; Lee, Y.-S. Base Effects on Fabrication of Silver Nanoparticles Embedded Silica Nanocomposite for Surface-Enhanced Raman Scattering (SERS). *J. Nanosci. Nanotechnol.* **2011,** *11*, 579-583.

(82) Jiang, P.; Deng, K.; Fichou, D.; Xie, S. S.; Nion, A.; Wang, C. STM imaging ortho- and para-fluorothiophenol self-assembled monolayers on Au(111). *Langmuir* **2009,** *25*, 5012-5017.

(83) Pieczonka, N. P.; Aroca, R. F. Single molecule analysis by surfaced-enhanced Raman scattering. *Chem. Soc. Rev.* **2008,** *37*, 946-954.

(84) Jalani, G.; Lee, S.; Jung, C. W.; Jang, H.; Choo, J.; Lim, D. W. Controlled biohybrid nanoprobes with silver nanoparticle clusters for Raman imaging. *Analyst* **2013,** *138*, 4756-4759.

(85) Huang, P.-J.; Chau, L.-K.; Yang, T.-S.; Tay, L.-L.; Lin, T.-T. Nanoaggregate-Embedded Beads as Novel Raman Labels for Biodetection. *Adv. Funct. Mater.* **2009,** *19*, 242-248.

(86) Chen, G.; Wang, Y.; Yang, M.; Xu, J.; Goh, S. J.; Pan, M.; Chen, H. Measuring ensemble-averaged surface-enhanced Raman scattering in the hotspots of colloidal nanoparticle dimers and trimers. *J. Am. Chem. Soc.* **2010,** *132*, 3644-3645.

(87) Abbas, A.; Tian, L.; Kattumenu, R.; Halim, A.; Singamaneni, S. Freezing the self-assembly process of gold nanocrystals. *Chem. Commun.* **2012,** *48*, 1677-1679.

(88) Yoon, J. H.; Zhou, Y.; Blaber, M. G.; Schatz, G. C.; Yoon, S. Surface Plasmon Coupling of Compositionally Heterogeneous Core-Satellite Nanoassemblies. *J. Phys. Chem. Lett.* **2013,** *4*, 1371-1378.

(89) Steinigeweg, D.; Schutz, M.; Schlucker, S. Single gold trimers and 3D superstructures exhibit a polarization-independent SERS response. *Nanoscale* **2013,** *5*, 110-113.

(90) Halperin, A.; Buhot, A.; Zhulina, E. B. Sensitivity, specificity, and the hybridization isotherms of DNA chips. *Biophys. J.* **2004,** *86*, 718-730.

(91) Pardue, H. L. The inseparable triad: analytical sensitivity, measurement uncertainty, and quantitative resolution. *Clin. Chem.* **1997,** *43*, 1831-1837.

(92) Chen, Y.; Cai, J.; Xu, Q.; Chen, Z. W. Atomic force bio-analytics of polymerization and aggregation of phycoerythrin-conjugated immunoglobulin G molecules. *Mol. Immunol.* **2004,** *41*, 1247-1252.

(93) Peluso, P.; Wilson, D. S.; Do, D.; Tran, H.; Venkatasubbaiah, M.; Quincy, D.; Heidecker, B.; Poindexter, K.; Tolani, N.; Phelan, M.; Witte, K.; Jung, L. S.; Wagner, P.; Nock, S. Optimizing antibody immobilization strategies for the construction of protein microarrays. *Anal. Biochem.* **2003,** *312*, 113-124.

(94) Spitznagel, T. M.; Clark, D. S. Surface-Density and Orientation Effects on Immobilized Antibodies and Antibody Fragments. *Nat. Biotechnol.* **1993,** *11*, 825-829.

(95) Lee, S.; Kim, S.; Malm, J.; Jeong, O. C.; Lilja, H.; Laurell, T. Improved porous silicon microarray based prostate specific antigen immunoassay by optimized surface density of the capture antibody. *Anal. Chim. Acta* **2013,** *796*, 108-114.

(96) Gao, Z.; Hou, L.; Xu, M.; Tang, D. Enhanced colorimetric immunoassay accompanying with enzyme cascade amplification strategy for ultrasensitive detection of low-abundance protein. *Sci. Rep.* **2014,** *4*, 3966.

요 약

(국문 초록)

바이오 응용, 특히 면역 진단 분야 등에서의 다중 분석을 위한 요건은 신호간 중첩이 적으면서, 미량의 생체 표지자를 측정할 수 있는 민감도를 가지며, 정량성이 높은 프로브라 할 수 있다. 최근 표면 증강 라만 산란을 기반으로 한 면역 진단은 이러한 요건을 잠재하고 있다고 평가 되고 있으며, 뛰어난 다중도와 높은 감도로 인해 크게 주목을 받고 있다.

표면 증강 라만 산란을 기반으로 한 기술은 광안정성이 뛰어나고 나노플라즈모닉스와의 기술 융합을 바탕으로 매우 높은 감도를 갖는 것으로 많은 보고가 이루어져왔다. 그러나 바이오 응용 분야에 있어서 이를 실제 적용하기 위해서는 아직까지 개발 및 검증되어야 할 영역들이 있는데 이는 재현성, 폭넓은 정량적 역동범위(dynamic range) 등이라 할 수 있다. 이에 본 연구에서는 신뢰성이 있으며 감도가 높은 표면증강 라만산란 기반의 면역 분석 플랫폼을 개발하였다. 전립선암 특이항원을 모델 시스템으로 한 이 면역 분석 플랫폼은 1) 단일 입자 수준의 탐지 감도와 작은 입자간 편차를 갖는 고감도 표면증강 라만산란 분광활성 나노입자 (SERS dot), 그리고 2) 빠르고 감도가 좋으며 신뢰성 있게 2차원 면적을 분석하는 래스터 스캐닝 방식의 라만 측정의 두 가지 전략을 통하여 신뢰성과 고민감도를 구현하고자 하였다.

첫 번째로 나노프로브로서 SERS dot 과 Ag-Au SS를 합성하고 이의 정량성과 민감도를 평가하였다. SERS dot 은 이미 잘 알려져 있는 형태의 입자로 실리카 중심에 표면처리를 통하여 수십-수백 개의 은 나노

입자를 도입하고 라만 신호를 주는 분자와 실리카 껍질을 도입함으로서 ensemble average 효과를 갖는다. 이에 따라 532 nm 의 여기광에 대하여 개별 입자를 식별할 수 있는 감도의 신호를 주는 것을 확인했으며, 이 입자는 100 초 이상의 연속적인 레이저 조사에 대해서도 광안정성을 유지하는 것으로 나타났다.

뿐만 아니라 고체 기질을 이용하여 어셈블리 형태를 갖는 Ag-Au SS (은껍질 형태 중심-금입자 위성 형태)의 이종 금속 나노프로브를 성공적으로 합성하였다. 고체 기질은 용액 상에서 합성할 때에 비하여 입자들의 뭉침을 방지하고 합성이 끝난 후 원하는 형태의 분리가 가능하도록 하는 편리성을 제공하였다. 이때 합성된 Ag-Au SS 나노프로브는 532, 647, 785 nm 여기광에 대하여 모두 105 이상의 증강 인자(EF)를 나타내었으며 특히 785 nm의 근적외선 영역의 여기광에 대하여 좁은 분포의 높은 신호를 보였다. 3차원적인 SERS hot spot 의 분포로 인하여 이러한 재현성과 민감도가 나타나는 것으로 평가되었으며, 살아있는 실험 쥐에 주입하여 나노프로브의 신호를 측정하는데 성공하였다.

두 번째로 정량적인 칩 분석 방법을 연구를 통해 2차원 전영역에 대한 빠르고 신뢰성 있는 분석 방법을 제안하였다. 가장 널리 이용되고 있는 현미경 타입의 공초점 라만 시스템은 대부분 2차원 면적에 대하여 점스캔 방식으로 측정을 하게 되는데, 이는 1 μm 사이즈의 빔 포인트를 이용하므로 공간 분해능과 민감도가 뛰어난 반면, 넓은 영역에 대한 측정에는 상당한 제한이 있다. 따라서 대안으로서 민감도를 유지하면서 넓은 영역에 대한 측정을 위하여 래스터 스캔 방식의 2차원 분석을 도입하고, 기존 방법과의 분석 결과를 비교하였다. 래스터 스캔 방식은 약 1000 배 빠르게 측정하더라도 3배 정도의 민감도 차이만을 나타내는 것으로 평가되었다. 또한 이 방식은 매우 선형적으로 입자

농도에 따른 신호 세기를 측정하였으며, 다중정량분석에도 우수한 선형성을 나타내었다.

마지막으로 SERS dot과 래스터 스캔 방식의 라만 고속 측정 시스템을 이용하여 SIA 플랫폼을 완성하였다. SERS dot의 실리카 껍질은 입자에 생체 적합성 및 물리·화학적 안정성을 부여하며 추후에 입자 표면을 처리할 때 다루기가 매우 편리하게 하였다. 따라서 SERS dot 표면에 추적용 항체를 고정하였고, 슬라이드 글라스에 또 포획용 항체를 고정하여 항원이 존재하는 경우 면역 복합체를 형성함으로써 SERS 신호를 주게 하였다. 추적용 항체 및 포획자 항체를 고정하는 방법은 모두 형광 표지된 항체를 이용하여 최적화된 조건을 확립하였다. 최종적으로 개발된 SIA 플랫폼은 전립선암 특이항원을 ~0.11 pg/mL 의 고감도로 검출하였고, 5자리수의 넓은 역동 범위를 갖는 것으로 평가되었다. 또한 이 플랫폼은 환자 혈액에 대하여도 민감하고 넓은 범위의 검출이 가능하도록 하였다. 이로써 본 연구의 결과는 우수하고 기능이 뛰어나면서도 비용-효율적인 다중 분석 플랫폼으로서의 가능성을 보였다고 하겠다.

주요어 : 표면 증강 라만 산란, 면역 분석법, 나노프로브, 다중 분석, 근적외선 나노프로브, 정량분석, 대면적 스캔, 래스터 스캔, 대면적 라만 분석, 전립선암 특이항원, 재현성, 민감도

학 번 : 2011-21586